The Aeronautical Journal (2026), 1–31
doi:10.1017/aer.2026.10234

ROYAL AERONAUTICAL SOCIETY

RESEARCH ARTICLE

UAV icing: system identification of leading-edge rime-ice effects on a small fixed-wing drone

Bogdan Løw-Hansen[1,2], Markus Lindner[1,2], Tor Arne Johansen[1], Richard Hann[1,2] and Christoph Deiler[3]

[1]Department of Engineering Cybernetics, Norwegian University of Science and Technology: Norges teknisk-naturvitenskapelige universitet, Trondheim, Norway
[2]Ubiq Aerospace AS, Trondheim, Norway
[3]DLR Institute of Flight Systems, Deutsches Zentrum für Luft- und Raumfahrt (DLR), Braunschweig, Germany
Corresponding author: Bogdan Løw-Hansen; Email: bogdan.l.hansen@ntnu.no

Received: 5 March 2026 UTC; **Revised:** 10 August 2026 UTC; **Accepted:** 10 August 2026 UTC

Keywords: aircraft stability and control; drone; flight testing; rime-ice; RPAS; small fixed-wing UAV; system identification; UAS; UAV icing

Abstract

As small fixed-wing unmanned (or uncrewed) aerial vehicles (UAVs) are increasingly deployed for long-endurance, beyond visual line-of-sight (BVLOS) missions, atmospheric icing has emerged as a critical operational hazard. One of the barriers to safe flight in these conditions is the lack of validated aerodynamic icing-degradation models, which are essential for developing robust mitigation strategies. This paper presents an experimental system identification study quantifying the effects of leading-edge wing icing on the flight characteristics of a Skywalker X8 UAV. Three-dimensional rime ice shapes were generated in an icing wind tunnel (IWT), digitised using photogrammetry, and reproduced via 3D printing for flight testing. Closed-loop excitation manoeuvres were flown at constant airspeed in clean and iced configurations, enabling reconstruction of aerodynamic coefficients and identification of quasi-steady coefficient models. The results show a clear increase in drag (a 50% increase in zero-lift drag coefficient), which roughly halves the maximum lift-to-drag ratio. Furthermore, the iced aircraft exhibits a 23% decrease in lift slope in the primary regime (angle-of-attack above 0°), a reduced static stability margin and degraded pitch and lift control effectiveness. Linearised analysis further shows a pronounced slowdown of the short-period and roll dynamics as well as reduced Dutch-roll damping. Overall, these models provide a crucial quantitative baseline to assess performance penalties and develop robust icing detection, envelope protection and guidance strategies for small fixed-wing UAVs operating in icing conditions.

Nomenclature

C_{D*}, C_{L*}	drag and lift coefficients
$C_{\{l*,m*,n*\}}$	body-axis moment coefficients
C_{T*}, C_{Q*}	propeller thrust and torque coefficients
$C_{\{X,Y,Z\}}$	body-axis force coefficients
D	drag force [N]
$\mathcal{D}$	propeller diameter [m]
$\mathbf{I}$	aircraft inertia tensor [kg m^2]
I_p	propeller moment of inertia [kg m^2]
$I_{\{x,y,z,xz\}}$	aircraft moments and product of inertia [kg m^2]
J	advance ratio [-]
$\mathbf{J}$	Fisher information matrix
L	lift force [N]
$\mathcal{N}(\boldsymbol{\mu}, \Sigma)$	multivariate Gaussian distribution
$\mathbf{P}$	parameter covariance matrix

© The Author(s), 2026. Published by Cambridge University Press on behalf of Royal Aeronautical Society. This is an Open Access article, distributed under the terms of the Creative Commons Attribution licence (https://creativecommons.org/licenses/by/4.0/), which permits unrestricted re-use, distribution and reproduction, provided the original article is properly cited.

Downloaded from https://www.cambridge.org/core. 28 Sep 2026 at 04:58:16, subject to the Cambridge Core terms of use.

P_*	power [W]
Q	propeller torque [Nm]
$\boldsymbol{R}$	SO(3) rotation matrix
S	wing planform area [m^2]
T	propeller thrust [N]
V_a	true airspeed [m/s]
X_u	speed-damping [N s m^{-1}]
Z_u	heave-damping [N s m^{-1}]
a_x, a_y, a_z	specific force in body axes [m/s^2]
b	wingspan [m]
$\bar{c}$	mean aerodynamic chord [m]
g	gravitational acceleration [m/s^2]
h	altitude [m]
k_α	blending steepness parameter [rad^{-1}]
m	aircraft mass [kg]
m_r	ice-rod mass [kg]
p, q, r	body-axis angular rates [rad/s]
p^*, q^*, r^*	nondimensional rates [-]
$\dot{p}, \dot{q}, \dot{r}$	body-axis angular accelerations [rad/s^2]
$\bar{q}$	dynamic pressure [Pa]
$\boldsymbol{q}$	attitude quaternion
$\boldsymbol{r}$	position vector [m]
u, v, w	body-axis linear velocities [m/s]
w_α	angle-of-attack blending weight [-]
$\boldsymbol{v}$	linear velocity vector [m/s]
$\boldsymbol{w}$	wind velocity vector [m/s]
x, y, z	body-axis position coordinates [m]
Δ_α	blending interval width [rad]
Ω_p	propeller angular speed [rad/s]
α_0	blending centre [rad]
α	angle-of-attack [rad]
β	angle of sideslip [rad]
δ_a, δ_e	aileron and elevator deflections [rad]
δ_{el}, δ_{er}	left and right elevon deflections [rad]
δ_t	normalised throttle [-]
ζ_{ph}	phugoid damping ratio [-]
η_*	efficiency or scale factor [-]
$\boldsymbol{\theta}$	model parameter vector
μ	mean value
ρ	air density [kg/m^3]
σ	standard deviation
ϕ, θ, ψ	Euler roll, pitch, yaw angles [rad]
$\boldsymbol{\omega}$	angular rate vector [rad/s]
ω_{ph}	phugoid natural frequency [rad/s]
$_a$	aerodynamic subscript
$_w$	wind subscript
*	trimmed state superscript
$(\cdot)^+, (\cdot)^-$	high- and low-α regimes in blended model
{b}	body frame
{n}	north-east-down frame

1.0 Introduction

The operational envelope of small fixed-wing unmanned aerial vehicles (UAVs) is rapidly expanding to include high-intensity commercial logistics and year-round, beyond visual line-of-sight (BVLOS)

Downloaded from https://www.cambridge.org/core. 28 Sep 2026 at 04:58:16, subject to the Cambridge Core terms of use.

missions [1]. As these missions scale, extended exposure to environmental hazards, such as atmospheric in-flight icing, has emerged as a limiting factor [2]. While typical battery-powered multirotor flights are often restricted to 15–30 minutes, fixed-wing platforms can easily fly for hours [3]. This extended flight capability elevates atmospheric icing to a severe operational hazard. Several recent climatological assessments aimed at quantifying this threat indicate that low-altitude UAVs can encounter icing conditions at non-negligible rates, especially during winter months [4, 5].

Although the hazard of atmospheric icing has been extensively studied and mitigated in general aviation, these traditional frameworks cannot be directly applied to smaller, unmanned platforms. Aerodynamically, small UAVs operate at significantly lower Reynolds numbers and employ much thinner aerofoil sections than conventional aircraft, making them inherently more sensitive to the performance penalties of ice accretion and surface contamination [6, 7]. Beyond these aerodynamic differences, the direct transfer of conventional physical ice protection systems (IPSs) to small fixed-wing UAVs remains constrained by stringent size, weight and power (SWaP) limitations [6, 8]. While these constraints do not preclude icing mitigation altogether, they typically restrict IPS usage, such as allowable duty cycles or spatial coverage. Consequently, small UAVs (less than 25 kg) can benefit greatly from information-driven strategies that adapt guidance, navigation and control (GNC) and IPS behaviour based on the aircraft's aerodynamic state, rather than relying on predefined anti-icing and de-icing cycles. Successfully implementing such strategies requires the flight controller to recognise ice accretion in flight, making an ice detection system (IDS) a critical prerequisite. Although the latest literature reviews highlight the availability of various IDS technologies [9, 10], their direct integration into small UAVs remains challenging. Consequently, since existing commercial sensors are often prohibitively expensive or exceed allowable SWaP budgets, there is still a need for alternative detection methodologies tailored specifically for lightweight aircraft.

Accurate aerodynamic modelling of icing effects can therefore be used as a tool to enable safe and robust UAV operations in icing conditions. Model-based detection, decision support and adaptive control strategies all presuppose the availability of reliable rigid-body models that capture how ice accretion alters aerodynamic forces, moments and dynamic modes. For manned aircraft, this need has long been recognised. Previous work has shown that icing effects can be incorporated into flight dynamics models through structured parameter extensions [11], later refined into regime-dependent Δ-model frameworks with explicit stall and separation representations [12, 13]. These modelling concepts, supported by extensive icing wind tunnel (IWT) and flight-test campaigns, have enabled detailed analysis of icing-induced changes in stability and control characteristics for general aviation aircraft [14–16].

While these foundational methodologies provide a vital reference, their specific aerodynamic results cannot be directly transferred to smaller unmanned platforms. In contrast to large transport aircraft, (lighter) business jets or regional aircraft, small UAVs possess unique airframe configurations (e.g. position and design of wing(s) and empennage) and fundamentally different baseline mass properties. Specifically, the relationship between vehicle size and accreted ice mass is disproportionate for smaller UAVs, leading to unique dynamic penalties. Therefore, although the system identification techniques developed for manned aviation offer an excellent methodological baseline, the dynamic response of iced UAVs remains an open research question that must be evaluated using dedicated flight-test data.

To date, experimentally identified icing models for small fixed-wing UAVs remain largely absent from the open literature. A recent review of flight-test-based system identification studies for small UAVs [17, Table 2] shows that while numerous clean-aircraft models exist, such as those developed for model-based navigation [18], none explicitly address atmospheric icing. Existing UAV icing research has instead focused primarily on static aerodynamic degradation and ice morphology [19–22], or on propulsion system effects such as propeller icing [23–28]. Although these studies consistently demonstrate substantial performance penalties, they do not quantify how icing alters the flight dynamic modes and control characteristics for small fixed-wing UAVs.

Several authors have proposed model-based icing detection and adaptive control strategies as surveyed in Refs [9, 10], and recent large-scale efforts such as work done within the Horizon 2020 project SENS4ICE [29] further highlight the importance of model-based decision support. However, these

Downloaded from https://www.cambridge.org/core. 28 Sep 2026 at 04:58:16, subject to the Cambridge Core terms of use.

Table 1. *Physical properties of the flight-ready Skywalker X8 UAV*

Property		Value
Mass	m	3.730 kg
Moment of inertia	I_x	0.335 kg m^2
—	I_y	0.140 kg m^2
—	I_z	0.400 kg m^2
Product of inertia	I_{xz}	−0.029 kg m^2
Mean chord length	$\bar{c}$	0.36 m
Wing span	b	2.10 m
Planform area	S	0.75 m^2
Sweep angle	–	28.3°



Figure 1. *Skywalker X8 UAV takeoff during the flight campaign near Trondheim, Norway.*

approaches fundamentally rely on the availability of accurate rigid-body aerodynamic models for iced configurations. For small fixed-wing UAVs, such models have yet to be established experimentally, so recent research on flight control in icing conditions [30–32] has relied on models with limited validation.

Motivated by this gap, the present work addresses the following research questions (RQs):

RQ1: How does wing icing alter the aerodynamics of a small fixed-wing UAV?

RQ2: Can quasi-steady models capture these icing-induced changes?

RQ3: What are the implications for IPS/IDS and GNC of small fixed-wing UAVs?

To answer these questions, we perform a flight-test-based system identification study of the Skywalker X8 UAV (Figure 1 and Table 1) in clean and wing-iced configurations. Artificial ice shapes are produced in an IWT (Section 2) and installed on the airframe; the resulting rigid-body changes are quantified and accounted for in the analysis (Section 3). Using a structured quasi-steady aerodynamic model (Section 4) and output-error identification on dedicated manoeuvres (Section 5), we quantify icing-induced aerodynamic changes and assess model adequacy and identification challenges. Results and implications are presented in Sections 6–8.

2.0 Creation of the artificial ice shapes

2.1 Icing wind tunnel campaign

The artificial ice shapes used for the comparative clean/iced flight tests were generated during an IWT campaign at the VTT Technical Research Centre of Finland in Helsinki [33]. The facility is an open-loop tunnel with a 700 mm x 700 mm test section. The 3D wing segment was mounted in an open-jet configuration at the test section exit using external brackets (see Figure 2). The wing was fixed at an

Downloaded from https://www.cambridge.org/core. 28 Sep 2026 at 04:58:16, subject to the Cambridge Core terms of use.

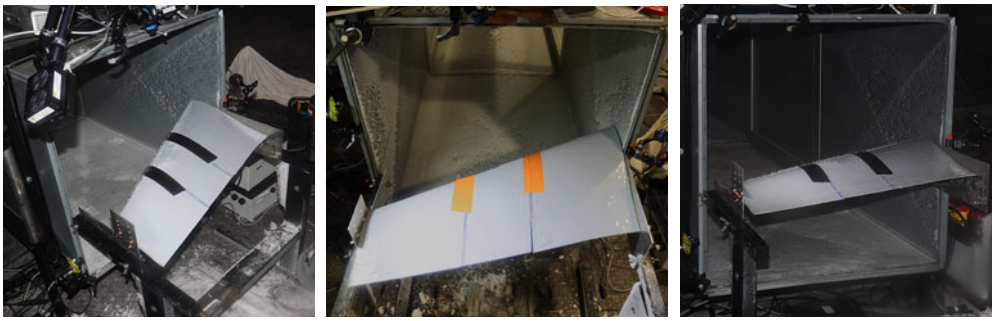

(a) Side view (b) Top view (c) Back view

Figure 2. *Placement of the wing in the IWT during accretion experiments. The visible chord-wise lines mark the boundaries of three splittable wing sections, with the central 150 mm portion serving as the isolated test segment for representative ice extraction. (The tape covering the splits was changed between experiments).*

angle-of-attack of 4°, selected as a representative cruise condition derived from prior flight-test campaigns with this UAV family [17, 34]. Previous characterisations of the facility's flow field revealed substantial spatial variability in the liquid water content (LWC) outside the tunnel core [35]. However, the calibration also identified a 200 mm × 100 mm central region exhibiting low LWC variation. To ensure uniform droplet exposure and minimise localised trajectory distortions near the mounting brackets, the representative test segment was limited to a width of 150 mm (as can be recognised by the chord-wise markings on the wing in Figure 2).

In defining the meteorological conditions for this uniform test region, the continuous maximum icing conditions detailed in FAA Part 25, Appendix C [36] were used as a guiding framework. While these conditions provide a widely recognised baseline for manned aviation, their representativeness for the lower-altitude regimes of small UAVs remains an open research question [6]. Specifically, the IWT target conditions were set to an LWC of 0.52 g/m^3 with a median volume diameter (MVD) of 27.4 μm at −10 °C. Although this LWC is higher than the nominal Appendix C continuous maximum envelope for this droplet size (0.26 g/m^3), a more substantial ice accretion was deliberately targeted. This over-scaling ensures that the resulting geometry is representative of intentionally pronounced rime ice accretions. Consequently, the ice generates an aerodynamic penalty of sufficient magnitude to clearly overcome flight-test measurement noise and state-estimation uncertainties, such as the $\sigma_\alpha = 0.6°$ angle-of-attack variance detailed in subsection 5.4, allowing the clean and iced states to be robustly distinguished in the final identified models.

The tunnel airspeed was maintained at 25 m/s, slightly above the UAV's nominal cruise speed of 18 m/s, to ensure consistency with a concurrent experimental baseline. Furthermore, to simulate realistic prolonged exposure to an icing environment during BVLOS operations, the accretion duration was set to 20 min. At this selected airspeed, a 20-minute duration yields a theoretical cloud traverse distance close to the standard 17.4 NM (32.2 km) horizontal extent defined for Appendix C continuous maximum encounters (21.5 min at 25 m/s).

2.2 Photogrammetry digitisation and 3D printing

After the ice accretion run, the middle segment was detached and trimmed to retain a 118 mm spanwise ice extent. To capture its complex geometry, the ice shape was digitised into a full 3D model using the photogrammetry methodology detailed in Ref. [35]. By comparing the physical weight of the sample to the volume of the 3D model, the density of the accreted ice was computed to 0.4 g/cm^3, which falls within the realistic range of 0.1 to 0.9 g/cm^3 reported in Ref. [37]. A comparison between the original ice, the digitised model and the resulting print is shown in Figure 3.

Downloaded from https://www.cambridge.org/core. 28 Sep 2026 at 04:58:16, subject to the Cambridge Core terms of use.

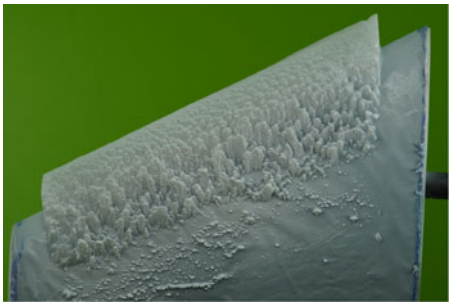

(a) Original rime ice shape.

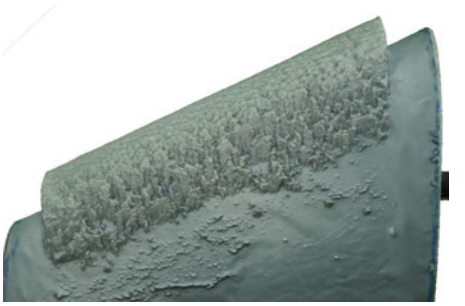

(b) Photogrammetry model.

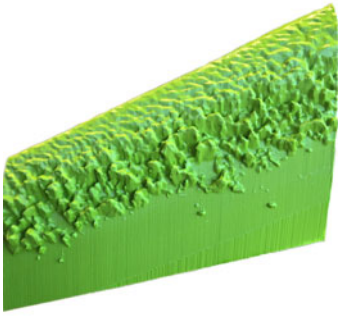

(c) Final 3D printed shape.

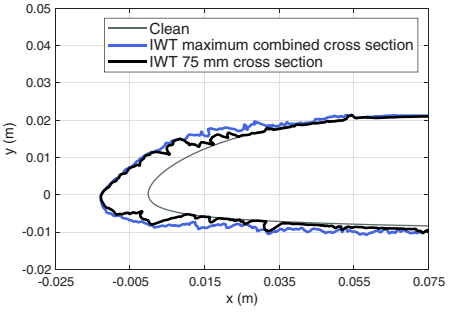

(d) Ice shape 2D cross sections.

Figure 3. *Comparison of the original ice shape created in the IWT and the digitised photogrammetry ice shape.*

The final flight-test ice shapes were produced by additive manufacturing (3D printing). Since only a 118 mm spanwise segment was available, the digitised ice was linearly scaled according to the chord length variation along the entire wing span, with six segments per wing. Right-wing segments were obtained by mirroring about the chordwise axis. While this linear scaling assumption provides a baseline for system identification experiments, true spanwise ice accretion on swept wings is more complex. As demonstrated in large-scale swept-wing icing studies [38, 39], the ice shape depends on the variations in wing geometry, such as changes in the leading-edge radius.

Furthermore, testing swept-wing segments in confined wind tunnel environments can alter the spanwise stagnation and attachment line locations. This effect has been shown to be significant for large commercial transport wings and requires explicit computational matching procedures to correct the flow over truncated models [40]. For the work presented here, where the goal is a representative ice shape for system identification, these corrections are deemed less critical given the other limitations of the ice shape generation method – notably the deliberately over-scaled LWC and the linear spanwise scaling of a single 118 mm segment.

The mass of the segments was matched to the total estimated ice mass by adjusting infill settings during 3D printing. Table 2 summarises the estimated segment masses from the fitted 3D model and the corresponding printed masses; small segment-level deviations are expected due to chord scaling, print tolerances and discrete infill settings, while the total mass match is preserved. Printing was performed using an Ultimaker S5 3D-printer. The installed ice shapes are shown in Figure 4. The total added mass was 420 g (210 g per wing), resulting in a 6 mm forward shift of the centre of gravity (CG) measured by a 3-point balance and weight meter.

As seen in Figure 4, the installed ice shapes introduce a sharp geometric edge at the inboard root, which is expected to generate localised flow separation and artificially contribute to the identified drag penalty. Conversely, this artificial representation does not cover secondary airframe components that

Downloaded from https://www.cambridge.org/core. 28 Sep 2026 at 04:58:16, subject to the Cambridge Core terms of use.

Table 2. *Estimated and 3D-printed ice-segment masses (rounded to the nearest gram)*

	Seg. 1	Seg. 2	Seg. 3	Seg. 4	Seg. 5	Seg. 6	Total
Estimated	62 g	62 g	34 g	24 g	18 g	13 g	213 g
3D printed	58 g	48 g	34 g	28 g	24 g	18 g	210 g



(a) Lower-side view of installed ice shapes.



(b) Upper-side view of installed ice shapes.

Figure 4. *Ice shapes used for the iced configuration flights, installed continuously from root to tip. The complete leading-edge accretion on each wing consists of six 3D-printed segments: one black at the root, three coloured in the middle and two black near the tip.*

would accrue ice in practice, omitting realistic drag contributions. To perfectly isolate the aerodynamic effects of leading-edge accretion, future experimental iterations should incorporate spanwise edge smoothing and/or full-airframe icing models.

3.0 Rigid-body changes due to wing icing

Leading-edge icing affects the identified flight dynamics not only through aerodynamic degradation, but also through rigid-body changes. The added ice mass is distributed away from the fuselage centreline, increasing the moments of inertia and shifting the CG forward. To capture these effects, the accretion is approximated by six cylindrical rods per wing, attached symmetrically along the span as illustrated in Figure 5. Each rod contribution is shifted to the aircraft CG using the parallel-axis theorem

$$I_{UAV} = I_{rod} + m_r d^2, \tag{1}$$

where m_r is the rod mass and d is the perpendicular distance from the rod centroid to the axis of rotation.

The total mass increased from 3.73 to 4.15 kg, corresponding to an increase of 11%. The ice shapes are installed symmetrically about the aircraft x–z plane (left–right symmetry), such that the added mass does not influence I_{xy} and I_{yz}. The vertical offset of the added ice relative to the x–y plane is assumed negligible, implying a negligible contribution to I_{xz}; consequently, the products of inertia are assumed

Downloaded from https://www.cambridge.org/core. 28 Sep 2026 at 04:58:16, subject to the Cambridge Core terms of use.

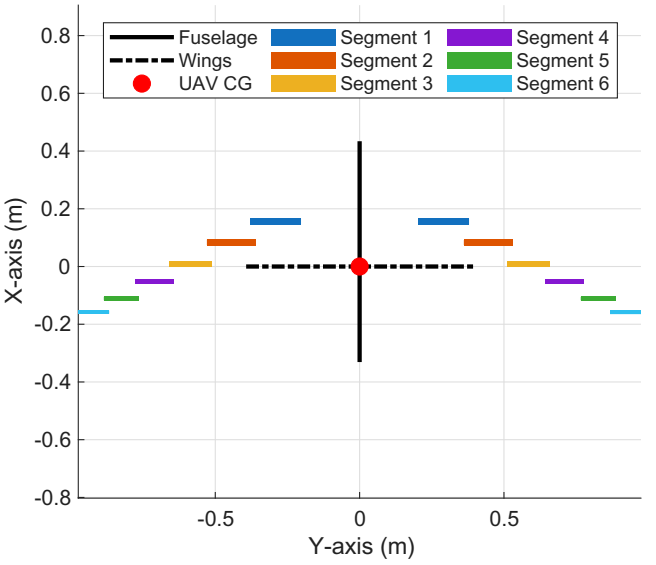

Figure 5. *Relative placement of the ice-rod segments used for modelling rigid-body changes.*

unchanged. The resulting inertia tensors are given by

$$\mathbf{I}_{\text{clean}} = \begin{bmatrix} 0.335 & 0 & -0.029 \\ 0 & 0.140 & 0 \\ -0.029 & 0 & 0.400 \end{bmatrix} \text{kg m}^2, \ \mathbf{I}_{\text{iced}} = \begin{bmatrix} 0.480 & 0 & -0.029 \\ 0 & 0.145 & 0 \\ -0.029 & 0 & 0.550 \end{bmatrix} \text{kg m}^2 \quad (2)$$

While a higher-fidelity volumetric integration of the exact 3D ice shape or experimental validation via swing testing could yield more precise mass properties, the expected gain is minimal relative to the added uncertainty. Because the added ice mass is concentrated at the leading edge, its contribution to the aircraft's total inertia is heavily dominated by its distance from the CG ($m_i d^2$), rather than its local geometric details. Consequently, the difference between an exact 3D volume integration and the rod-segment approximation is negligible for the overall rigid-body dynamics. Furthermore, conducting physical swing tests (e.g. via a bifilar pendulum) on fixed-wing UAVs introduces non-negligible aerodynamic added-mass effects due to entrained air, which inherently complicates the measurements [41]. Correctly isolating these effects would require considerable effort, which in this case is left for future work.

The CG location was measured using a dedicated CG balance rig, with all quantities referenced to a centre of origin (CO) coincident with the inertial measurement unit (IMU)/estimator frame. The measured longitudinal offsets are

$$\mathbf{r}^{\text{clean}}_{\text{CO}\to\text{CG}} = [0.110 \ 0 \ 0]^\top \text{ m}, \qquad \mathbf{r}^{\text{iced}}_{\text{CO}\to\text{CG}} = [0.116 \ 0 \ 0]^\top \text{ m},$$

corresponding to a forward shift of 6 mm. The CG was not measured along the vertical axis; the vertical offset is assumed unchanged and treated as a source of uncertainty.

Aerodynamic forces and moments are evaluated about the CG. The aerodynamic centre (AC) is assumed to coincide with the CG in both configurations. This simplifying assumption is reasonable because the CG is not expected to change during flight, and the distance between the true AC and the CG is small. From classical static stability theory [42, Chap. 4.9], the offset is proportional to the static margin:

$$x_{\text{ac}} - x_{\text{cg}} = -\bar{c}\frac{C_{m\alpha}}{C_{L\alpha}} \quad (3)$$

Downloaded from https://www.cambridge.org/core. 28 Sep 2026 at 04:58:16, subject to the Cambridge Core terms of use.

Based on the identified coefficients in subsection 6.4, this yields a theoretical offset of 2.7 cm in the clean case (with the AC located behind the CG).

Finally, the accreted ice modifies the effective reference geometry by changing the aerofoil geometry and increasing the chord length. Based on the reconstructed ice geometry, the mean aerodynamic chord increases from $\bar{c} = 0.36$ to $\bar{c}_{\text{ice}} = 0.38$ m, and the projected wing planform area increases from $S = 0.75$ to $S_{\text{ice}} \approx 0.81$ m^2. These iced-geometry values are reported for completeness; however, to ensure direct comparability between clean and iced results, all aerodynamic coefficients in this paper are nondimensionalised using the clean reference quantities $(S, \bar{c}, b)$ for both configurations.

4.0 Aerodynamic modeling

This section outlines the methodology for aerodynamic system identification. It details the procedures required to isolate bare-airframe aerodynamics from propulsive effects, reconstruct aerodynamic forces and moments from flight kinematics, and formulate a model structure capable of characterising both the clean and iced configurations.

4.1 Computed coefficients from flight data

System identification is performed by fitting parametric coefficient models to equivalent aerodynamic coefficients reconstructed from flight data. The reconstruction follows Ref. [17] and uses IMU-specific force measurements expressed in the body frame and transformed to the CG (a_x, a_y, a_z), together with gyroscope body rates (p, q, r). The IMU measurements are corrected using the bias estimates from the ArduPilot's extended Kalman filter (EKF) before any transformations are applied. Angular accelerations $(\dot{p}, \dot{q}, \dot{r})$ are obtained from (p, q, r) using a 5-point local quadratic least-squares differentiator [43]. The measurements are scaled by dynamic pressure $\bar{q} = \frac{1}{2}\rho V_a^2$, where V_a is the true airspeed at CG and ρ is the air density. Using these quantities (with thrust and torque compensation from subsection 4.2), the reconstructed coefficients are computed as:

$$C_X = \frac{ma_x - T}{\bar{q}S}, \tag{4a}$$

$$C_Y = \frac{ma_y}{\bar{q}S}, \tag{4b}$$

$$C_Z = \frac{ma_z}{\bar{q}S}, \tag{4c}$$

$$C_l = \frac{1}{\bar{q}Sb}\left[I_x\dot{p} - I_{xz}(pq + \dot{r}) + \left(I_z - I_y\right)qr + Q\right], \tag{4d}$$

$$C_m = \frac{1}{\bar{q}S\bar{c}}\left[I_y\dot{q} + \left(I_x - I_z\right)pr + I_{xz}\left(p^2 - r^2\right) + I_p\Omega_p r\right], \tag{4e}$$

$$C_n = \frac{1}{\bar{q}Sb}\left[I_z\dot{r} - I_{xz}(\dot{p} - qr) + \left(I_y - I_x\right)pq - I_p\Omega_p q\right]. \tag{4f}$$

The propeller gyroscopic coupling terms $I_p\Omega_p r$ and $-I_p\Omega_p q$, where I_p is the propeller inertia and Ω_p is the propeller speed, are retained in Equations (4e) and (4f), whereas the inertial torque term proportional to the propeller angular acceleration $I_p\dot{\Omega}_p$ is omitted. In normal flight, this can often be justified since the motor speed is fairly constant. Moreover, the motor-speed measurement is available at only 10 Hz, and numerical differentiation introduces uncertainty that outweighs the benefit of including this term. Nevertheless, in settings where Ω_p is not measured and is instead inferred from electrical power and efficiency models, including $I_p\dot{\Omega}_p$ may be beneficial; this was considered in Ref. [17].

Downloaded from https://www.cambridge.org/core. 28 Sep 2026 at 04:58:16, subject to the Cambridge Core terms of use.

Table 3. *Thrust and torque coefficients*

C_T		C_Q	
C_{T0}	0.1537	C_{Q0}	0.0084
C_{T1}	−0.1059	C_{Q1}	0.0100
C_{T2}	−0.0967	C_{Q2}	−0.0200

Table 4. *Propeller parameters*

Property		Value
Diameter	$\mathcal{D}$	0.3556 m (14”)
Moment of inertia	I_p	3.46×10^{-4} kg m^2
Thrust scale	η_T	1.00/0.81 (Clean/Iced)
Torque scale	η_Q	1.00/0.83 (Clean/Iced)

4.2 Propulsion and actuator models

The propulsion model provides the thrust and torque compensation necessary to separate airframe drag from thrust-induced acceleration. The torque and thrust coefficients, C_Q and C_T, are represented as second-order polynomials of the nondimensional advance ratio J:

$$J = \frac{2\pi V_a}{\Omega_p \mathcal{D}}, \tag{5}$$

$$C_Q(J) = C_{Q0} + C_{Q1}J + C_{Q2}J^2\,, \tag{6}$$

$$C_T(J) = C_{T0} + C_{T1}J + C_{T2}J^2\,, \tag{7}$$

where $\mathcal{D}$ is the propeller diameter, V_a is the airspeed and Ω_p is the propeller angular speed.

To account for configuration-dependent installation effects, the dimensional torque and thrust are computed with empirical scaling factors, η_Q and η_T:

$$Q = \eta_Q \frac{\rho \mathcal{D}^5}{4\pi^2} C_Q(J)\Omega_p^2\,, \tag{8}$$

$$T = \eta_T \frac{\rho \mathcal{D}^4}{4\pi^2} C_T(J)\Omega_p^2\,. \tag{9}$$

The Skywalker X8 UAV used in this study was flown with an Aero-naut CAM Z Carbon 14x8 folding propeller. The baseline polynomial parameters, in Tables 3 and 4, were identified from isolated wind-tunnel experiments following the methodology in Ref. [28].

For the clean UAV configuration, it is assumed that the installed pusher propeller behaves sufficiently similarly to the isolated wind-tunnel tests. Therefore, the baseline models are used without scaling ($\eta_T = 1.0$, $\eta_Q = 1.0$). However, applying these uninstalled models directly to the iced configuration introduces significant physical inconsistencies. The iced airframe forces the powertrain into a regime where the polynomials identified in the wind tunnel over-predict the propulsive output. To quantify this discrepancy, two apparent operational efficiencies are defined based on the unscaled wind-tunnel models: the apparent electromechanical efficiency η_{mech} and the apparent overall propulsive efficiency η_{prop}:

$$\eta_{\text{mech}} = \frac{Q\,\Omega_p}{P_{\text{batt}}} \quad , \quad \eta_{\text{prop}} = \frac{T\,V_a}{P_{\text{batt}}}\,, \tag{10}$$

where P_{batt} is the power drawn from the battery, computed as the product of the measured voltage and current. Evaluating the mean of these ratios over the respective flights yields:

- Clean configuration: $\eta_{\text{mech}} \approx 0.8959$, $\eta_{\text{prop}} \approx 0.6454$.
- Iced configuration: $\eta_{\text{mech}} \approx 1.0809$, $\eta_{\text{prop}} \approx 0.7962$.

Downloaded from https://www.cambridge.org/core. 28 Sep 2026 at 04:58:16, subject to the Cambridge Core terms of use.

Table 5. *Model parameters for a 2nd order servo system controlling the elevons*

Natural frequency	Damping	Input delay	Deflection range
100 rad/s	0.707	0.12 s	± 19°

The unphysical iced apparent electromechanical efficiency ($\eta_{\text{mech}} = 1.0809$) proves that the uninstalled propeller model over-predicts loads when extrapolated to the iced UAV configuration. This notable loss of propulsive performance could be linked to the pusher propeller ingesting the turbulent wake generated by the sharp inboard edges of the artificial ice shapes, motivating the use of smoothed spanwise transitions for future experiments. Aerodynamically, because the propeller operates in this momentum deficit, using the true airspeed (V_a) to compute the advance ratio (J) neglects the locally reduced inflow velocity, mathematically inflating the predicted torque and thrust. Lacking an in-flight thrust meter to decouple these aero-propulsive effects, the uncorrected output error (OE) algorithm would erroneously absorb this inflated thrust and torque into overestimated aerodynamic drag and rolling moments. Indeed, initial estimations using unscaled models yielded a power penalty equal to 230% of the measured change.

To prevent this, the iced powertrain model is anchored to the clean apparent efficiency baseline using scaling factors $\eta_T = 0.8106$ and $\eta_Q = 0.8289$. Although true propeller efficiency likely degrades further in the turbulent iced wake, making additional corrections without direct thrust measurements would be arbitrary. Thus, this baseline anchoring is a deliberate engineering choice: it neutralises the propulsive over-prediction and forces any true propulsive degradation to be absorbed by the identified aerodynamic coefficients. As will be demonstrated in subsection 6.6, this strategy yields a representative systemic model that reasonably bounds the modelled power penalty due to ice accretion.

The servo delay was determined from clean experiment data by computing the mean lag between the initial elevator step inputs and the resulting pitch-rate response, while the natural frequency and damping were carried over from Ref. [17]. The resulting servo model parameters are listed in Table 5.

4.3 Aerodynamic coefficient model

The coefficient parametrisation determines which aerodynamic states are required for model evaluation and simulation. A classical representation in angle-of-attack α, angle of sideslip β, nondimensional angular rates and elevator/aileron inputs is adopted to align with the aircraft icing literature, where changes in lift and drag are commonly reported as functions of angle-of-attack and ice accretion [11–13, 19, 21, 44–46].

The aerodynamic angles are computed starting from the body-axis velocity and the estimated wind, in component form:

$$\begin{bmatrix} u_a \\ v_a \\ w_a \end{bmatrix} = \begin{bmatrix} u - u_w \\ v - v_w \\ w - w_w \end{bmatrix}, \tag{11}$$

with true airspeed V_a and aerodynamic angles computed as:

$$V_a = \sqrt{u_a^2 + v_a^2 + w_a^2}, \quad \alpha = \tan^{-1}\left(\frac{w_a}{u_a}\right), \quad \beta = \sin^{-1}\left(\frac{v_a}{V_a}\right). \tag{12}$$

The nondimensional angular rates are given by:

$$p^* = \frac{pb}{2V_a}, \quad q^* = \frac{q\bar{c}}{2V_a}, \quad r^* = \frac{rb}{2V_a}.$$

Downloaded from https://www.cambridge.org/core. 28 Sep 2026 at 04:58:16, subject to the Cambridge Core terms of use.

The Skywalker X8 is a flying-wing UAV with right and left elevons (δ_{er}, δ_{el}), which are mapped to equivalent elevator and aileron deflections (δ_e, δ_a) by:

$$\begin{bmatrix}\delta_e\\ \delta_a\end{bmatrix} = \frac{1}{2}\begin{bmatrix}1 & 1\\ -1 & 1\end{bmatrix}\begin{bmatrix}\delta_{er}\\ \delta_{el}\end{bmatrix} \tag{13}$$

The model terms were selected using a stepwise regression algorithm applied to a candidate pool of linear, non-linear and coupled aerodynamic regressors. Initial modelling attempts with a globally smooth, quasi-steady longitudinal formulation produced convergent fits, but closer inspection of reconstructed coefficient trends (see Section 6) showed that a global linear model could not simultaneously fit the distinct lift, pitching-moment and drag curves at positive and negative angles of attack, suggesting a regime change near $\alpha \approx 0^\circ$. This is consistent with the break-point modelling approach for iced aircraft presented in Ref. [12].

Accordingly, the longitudinal model is represented by two regimes blended by a continuous weight w_α, defined as:

$$\mathrm{w}_\alpha = \frac{1}{1+\exp((\alpha-\alpha_0)k_\alpha)}, \qquad k_\alpha = \frac{2\log(9)}{\Delta_\alpha} \tag{14}$$

where the factor $2\log(9)$ is chosen so that the weight transitions from 0.9 to 0.1 over the interval Δ_α centered at α_0. In this case, the interval was set to $\Delta_\alpha = 0.0175\,\mathrm{rad} = 1^\circ$.

During the initial system identification, the centre of this transition (α_0) was treated as a free parameter and converged within a band around -2° and 0° for both configurations. However, allowing the break-point to wander within this range degraded the overall convergence and stability of the aerodynamic derivatives. To prevent this, α_0 was fixed at the data-driven consensus value of -0.02 rad (approximately -1.1°).

The two resulting regime models are denoted by superscripts $^+$ and $^-$ and are blended by w_α. Candidate break-point extensions were selected by inspection of coefficient trends and refined through trial-and-error to avoid numerical ill-conditioning. To keep the structure minimal, only coefficients required by the data were split between regimes; in particular, the lift and pitching-moment terms were split only for the iced configuration.

The resulting longitudinal model is:

$$C_L^+ = C_{L0} + C_{L\alpha}\alpha + C_{Lq}q^* + C_{L\delta e}\delta_e\,, \tag{15a}$$

$$C_L^- = C_{L0} + C_{L\alpha}^-\alpha + C_{Lq}q^* + C_{L\delta e}^-\delta_e\,, \tag{15b}$$

$$C_D^+ = C_{D0} + C_{Dq}q^* + C_{Dk1}C_L^+ + C_{Dk2}C_L^{+2}\,, \tag{15c}$$

$$C_D^- = C_{D0} + C_{Dq}^-q^* + C_{Dk1}^-C_L^- + C_{Dk2}^-C_L^{-2}\,, \tag{15d}$$

$$C_m^+ = C_{m0} + C_{m\alpha}\alpha + C_{mq}q^* + C_{m\delta e}\delta_e\,, \tag{15e}$$

$$C_m^- = C_{m0} + C_{m\alpha}^-\alpha + C_{mq}q^* + C_{m\delta e}^-\delta_e\,, \tag{15f}$$

$$C_L = (1-\mathrm{w}_\alpha)C_L^+ + \mathrm{w}_\alpha C_L^-\,, \tag{15g}$$

$$C_D = (1-\mathrm{w}_\alpha)C_D^+ + \mathrm{w}_\alpha C_D^-\,, \tag{15h}$$

$$C_m = (1-\mathrm{w}_\alpha)C_m^+ + \mathrm{w}_\alpha C_m^-\,. \tag{15i}$$

The lateral model is kept symmetric:

$$C_Y = C_{Y0} + C_{Y\beta}\beta + C_{Yp}p^* + C_{Yr}r^* + C_{Y\delta a}\delta_a\,, \tag{16a}$$

$$C_l = C_{l0} + C_{l\beta}\beta + C_{lp}p^* + C_{lr}r^* + C_{l\delta a}\delta_a\,, \tag{16b}$$

$$C_n = C_{n0} + C_{n\beta}\beta + C_{np}p^* + C_{nr}r^* + C_{n\delta a}\delta_a\,. \tag{16c}$$

Downloaded from https://www.cambridge.org/core. 28 Sep 2026 at 04:58:16, subject to the Cambridge Core terms of use.

Table 6. *Overview of performed system identification manoeuvres at 18 m/s*

Direction	Type	Pulse duration	Amplitude	Fitting	Validation clean/iced
Lateral	*1-2-1*	[0.1 s, 0.5 s]	[15°, 8°]	[3,3]	[3,3]/[3,3]
Lateral	Doublet	[0.1 s, 0.6 s, 3.0 s]	[15°, 8°, 5°]	[3,3,3]	[3,4,2]/[3,3,2]
Longitudinal	*3-2-1-1*	[0.2 s, 1.5 s]	[12°, 6°]	[3,3]	[3,3]/[2,2]
Longitudinal	Doublet	[0.3 s, 2.3 s]	[12°, 6°]	[3,3]	[2,3]/[5,3]

A thrust-related term was also tested in the drag model in Equations (15c) and (15d) similar to Ref. [17], but did not yield a meaningful improvement. In this case, it led to an unrealistically small zero-lift drag C_{D0}, implying significant drag reductions at low throttle. Thrust-related terms were therefore excluded from the final drag model.

5.0 Experiment setup

This section summarises the flight-test campaign and the data processing steps used to obtain measurements for the system identification process.

5.1 Flight campaign

Three flight tests were performed within a three-hour window on the morning of 19th November 2024 at Brenslan, Trondheim, Norway. Cruise altitude and airspeed were held at approximately 100 m and 18 m/s. The ground temperature was −2 °C, with estimated wind speeds of 2 m/s to 4 m/s. Each flight was powered by a 16 V, 8 Ah battery. Because the iced configuration increased power consumption, the iced dataset was split across two flights:

- Flight 1: Clean configuration (lateral and longitudinal manoeuvres).
- Flight 2: Iced configuration (lateral manoeuvres).
- Flight 3: Iced configuration (longitudinal manoeuvres).

In total, 106 manoeuvres were extracted: 53 in the clean configuration and 53 in the iced configuration. Each manoeuvre lasted 15–35 s yielding approximately 2200 s of experiment data. Roughly half of this dataset captures active dynamic excitations, while the remainder establishes the steady-state trim conditions before and after each manoeuvre.

5.2 Excitation manoeuvres and closed-loop execution

A set of pre-programmed excitation signals was injected by an onboard companion computer (Khadas Vim3) to achieve repeatable excitation while maintaining safe flight. A detuned custom attitude controller [47] ran on the companion computer in parallel with ArduPilot, utilising ArduPilot's guidance-driven roll and pitch references alongside the EKF-based attitude estimate. During the flight, a separate script on the companion computer injected the excitation signal offsets; consequently, the realised control surface deflections were superimposed on the closed-loop response rather than acting as clean open-loop perturbations.

The manoeuvre set follows standard flight system identification practice and consists of four manoeuvre families (lateral *1-2-1*, lateral doublet, longitudinal *3-2-1-1* and longitudinal doublet). Within these families, pulse durations and amplitudes were varied, giving nine distinct excitations in total; the full set is summarised in Table 6. The pulse parameters were selected based on the clean-aircraft campaign in Ref. [17]. Moreover, prior to flight testing, ground experiments were conducted to map pulse-width modulation (PWM) commands to elevon deflection angles, ensuring that the desired deflection angles are correctly translated from degrees to the commanded PWM.

Downloaded from https://www.cambridge.org/core. 28 Sep 2026 at 04:58:16, subject to the Cambridge Core terms of use.

Table 7. *Summary of primary data sources. All data were resampled to the reference EKF time series at 20 Hz*

Data type	Source	Logged frequency
Attitude, linear velocity	Estimated (ArduPilot EKF)	20 Hz (reference)
Acceleration and rate biases	Estimated (ArduPilot EKF)	20 Hz
Horizontal wind state	Estimated (ArduPilot EKF)	20 Hz
Acceleration, angular rate	Measured (ICM20602/ICM20948)	50 Hz
GNSS	Measured (Here3+)	5 Hz
Airspeed (pitot-static)	Measured (MS4525DO)	10 Hz
Motor speed	Measured (HW-BQ2017)	10 Hz
Battery voltage and current	Measured (Analog Power Module)	10 Hz
Control commands	Generated (Khadas Vim3)	25 Hz

For each configuration, 27 manoeuvres were used for parameter estimation and the remaining 26 manoeuvres were reserved for validation presented in Section 6.

Although the experiments were executed with stabilising feedback, the identification uses the measured plant data in the sense of 'direct' closed-loop identification, i.e. applying a prediction error method directly to input–output data while ignoring possible feedback. In the prediction-error framework, this approach remains consistent provided that the tracked reference sufficiently excites the relevant dynamics and the model structure is adequate [48, Chap. 13.4]. A detailed closed-loop perspective is given by Forssell and Ljung [49], and a recent flight-test application of closed-loop identification, albeit using a frequency-domain joint input–output approach, is discussed in Ref. [50].

5.3 Flight data processing and synchronisation

The Skywalker X8 flight stack is built around the Cube Orange autopilot running ArduPilot firmware. Logged signals include EKF-estimated attitude and velocity, EKF-estimated horizontal wind, inertial measurements from the IMU, global navigation satellite system (GNSS) position and velocity, pitot-static airspeed, motor speed, battery voltage and current and the injected control commands from the companion computer. A reference time base was established from the EKF velocity timestamps, yielding a sampling frequency of 20 Hz. All channels were resampled to this reference time base using linear interpolation. Table 7 summarises the primary data sources and their original sampling rates.

5.4 Estimator and sensor measurement limitations

While the EKF does not explicitly estimate vertical wind, several factors suggest that the resulting reconstructed aerodynamic angles remain suitable for comparative analysis. The experiments were conducted within a three-hour window on a day with light winds; as shown in Figure 6, the average horizontal wind magnitude varied by only 1 m/s between flights. Given that the vertical wind component in the atmospheric boundary layer is typically several orders of magnitude smaller than the horizontal component [51, Chap. 1.2], changes in the mean vertical bias between flights are expected to be negligible. As an order-of-magnitude check, a vertical wind shift of 0.1 m/s at $V_a \approx 18$ m/s would correspond to $\Delta\alpha \approx 0.3^\circ$.

Angle-of-attack α and sideslip β are not measured directly but are reconstructed from the EKF states, making them subject to estimation uncertainty. The computation involves the body velocities, wind velocities and attitude quaternion $[\boldsymbol{v}^{\mathrm{n}}, \boldsymbol{w}^{\mathrm{n}}, \boldsymbol{q}]$, which are first transformed to the body frame in CG and then used as shown in Equations (11) and (12). To quantify the output uncertainty, a Monte Carlo analysis was performed. Specifically, to determine the uncertainty in the angle-of-attack at the nominal trim

Downloaded from https://www.cambridge.org/core. 28 Sep 2026 at 04:58:16, subject to the Cambridge Core terms of use.

Table 8. *Averaged EKF state variances during system identification manoeuvres*

State	Clean variance	Iced variance	Unit
v_n	2.013×10^{-2}	2.111×10^{-2}	$(\text{m/s})^2$
v_e	2.020×10^{-2}	2.113×10^{-2}	$(\text{m/s})^2$
v_d	1.241×10^{-2}	1.227×10^{-2}	$(\text{m/s})^2$
w_n	1.243×10^{-2}	1.226×10^{-2}	$(\text{m/s})^2$
w_e	1.078×10^{-2}	1.082×10^{-2}	$(\text{m/s})^2$
q_0	4.642×10^{-5}	4.930×10^{-5}	–
q_1	7.603×10^{-6}	7.760×10^{-6}	–
q_2	7.611×10^{-6}	7.736×10^{-6}	–
q_3	3.175×10^{-5}	3.296×10^{-5}	–

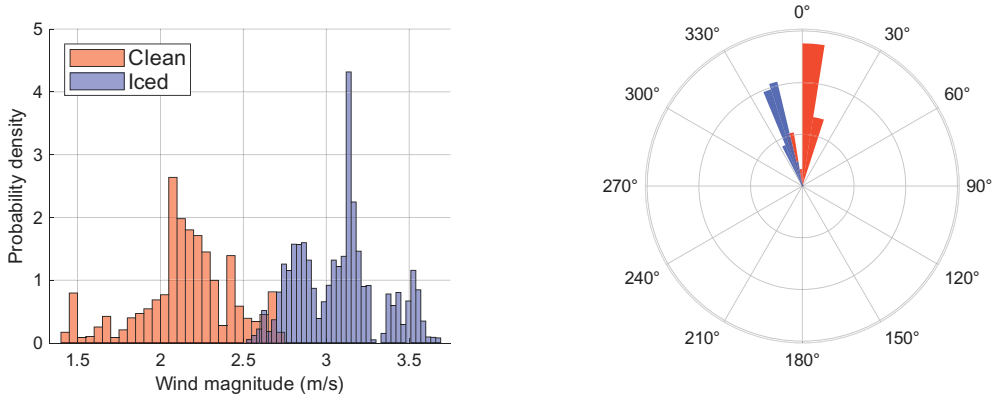

Figure 6. *Horizontal wind magnitude and direction estimated by the ArduPilot EKF during the experiments.*

condition, $N = 50000$ samples were drawn from a multivariate Gaussian distribution given by:

$$\boldsymbol{x} \sim \mathcal{N}\left(\boldsymbol{\mu}_{trim}, \Sigma_{EKF}\right) \tag{17}$$

where $\boldsymbol{x} = [\boldsymbol{v}^{\text{n}}, \boldsymbol{w}^{\text{n}}, \boldsymbol{q}]^T$ and $\boldsymbol{\mu}_{trim}$ represents the identified trimmed states for steady level flight at $V_a = 18$ m/s and zero wind. The diagonal covariance matrix Σ_{EKF} is populated by the mean EKF variances in Table 8 available from the recorded experiments. As the vertical wind component is not estimated by the ArduPilot EKF, its variance was approximated as the average of the estimated horizontal wind variances, $\sigma^2_{wd} = \frac{1}{2}(\sigma^2_{wn} + \sigma^2_{we})$.

Propagating these samples through the kinematic transformations and evaluating Equation (12) yields an aggregated standard deviation of $\sigma_\alpha \approx 0.6^\circ$. While a systematic bias in the angle-of-attack primarily affects the constant intercept terms (e.g. C_{L0}, C_{m0}), identified slope coefficients are less susceptible as they are constrained by the dynamic excitation during manoeuvres. Crucially, as the identical state-estimation and identification pipeline is applied to both configurations, the relative trends (deltas) between clean and iced parameters remain reliable, even if absolute magnitudes are subject to the baseline estimation uncertainty.

5.4.1 Pitot-static probe limitations

Although pitot-static measurements provide an independent airspeed source, simple pitot tubes are subject to well-known errors during highly dynamic manoeuvres, particularly at high-flow angles and under

Downloaded from https://www.cambridge.org/core. 28 Sep 2026 at 04:58:16, subject to the Cambridge Core terms of use.

Table 9. *Aerodynamic parameters and weighted outputs used during estimation*

Data (27 manoeuvres)	Parameter	Weighted outputs	Parameter	Weighted outputs
6 × longitudinal *3-2-1-1*		$z,\ V_a,\ \alpha$		$z,\ V_a,\ \beta$
6 × longitudinal doublet	$C_{D(*)}$	$\theta,\ q$	$C_{Y(*)}$	$\phi,\ \psi,\ p,\ r$
6 × lateral *1-2-1*	$C_{L(*)}$	$a_x,\ a_z$	$C_{l(*)}$	a_y
9 × lateral doublet	$C_{m(*)}$	$C_D,\ C_L,\ C_m$	$C_{n(*)}$	$C_Y,\ C_l,\ C_n$

Note: The listed outputs constitute the full set available; depending on manoeuvre and convergence behaviour, some output weights were disabled during fitting iterations.

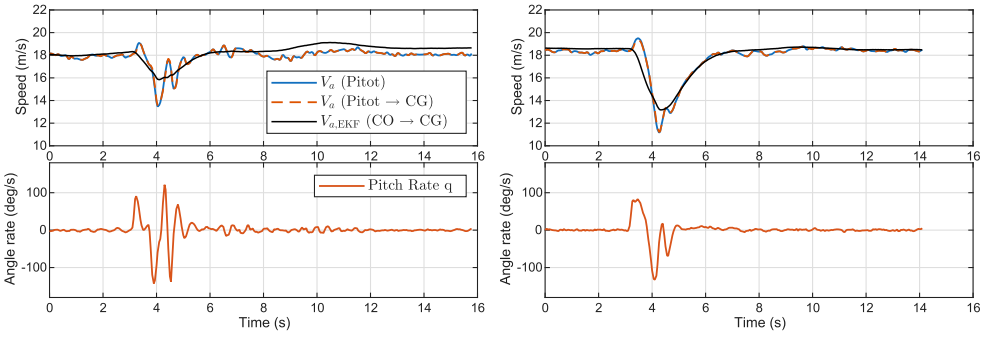

(a) Clean *3-2-1-1* maneuver example. (b) Iced *3-2-1-1* maneuver example.

Figure 7. *Measured and estimated airspeed comparison.*

unsteady conditions [52]. Specifically, rapid pitch variations can introduce nonphysical high-frequency oscillations into the measured airspeed as shown in Figure 7.

Because airspeed defines the dynamic pressure used to nondimensionalise all aerodynamic coefficients, propagating these sensor-induced oscillations would artificially contaminate the identified models. While transforming the measured airspeed to the CG, through the lever arm $\mathbf{r}_{pitot\to CO} = [-0.504\ 0\ 0.096]^\top$ m ($\mathrm{CO}_z \approx \mathrm{CG}_z$), accounts for the kinematic lever arm, it does not eliminate the observed aerodynamic artefacts. To mitigate this, the true airspeed used for dynamic pressure computation is instead derived from the EKF kinematic state estimates transformed to CG ($V_{a,\mathrm{EKF}}$). As shown in Figure 7, this estimator-derived airspeed accurately tracks the low-frequency trend while remaining insensitive to the high-frequency artefacts correlated with the pitch rate.

5.5 Weighted outputs and parameter groups

The aerodynamic parameters were estimated using a weighted output set comprising kinematic states, angular rates, accelerations and reconstructed force/moment coefficients. To reduce reliance on estimated states, body-axis velocities were not directly used as weighted outputs. Table 9 summarises the parameter groups and weighted outputs.

As demonstrated in Ref. [17], classic OE formulations [53] that weight only time-domain kinematic outputs can struggle to converge for small fixed-wing UAVs when direct flow angle measurements (e.g. from a five-hole probe) are unavailable, and estimated flow angles are used instead. Unlike large aircraft, which benefit from high inertial stability and high-fidelity direct air-data measurements, small UAVs are highly susceptible to wind gusts and must frequently rely on noisy, estimator-reconstructed states. This degrades the kinematic signal-to-noise ratio. To overcome these limitations, we employ a hybrid OE method that additionally weights the reconstructed aerodynamic coefficients during parameter fitting. Because these pseudo-measurements are derived from the same state and air-data sensors, their inclusion violates the maximum-likelihood assumption of uncorrelated measurement noise. Nevertheless,

Downloaded from https://www.cambridge.org/core. 28 Sep 2026 at 04:58:16, subject to the Cambridge Core terms of use.

this augmented formulation provides essential force and moment constraints, improving numerical conditioning and ensuring a physically consistent model.

The parameter estimation is performed using a Gauss–Newton output-error method. In each iteration, the parameter update $\Delta\boldsymbol{\theta}$ is obtained by solving

$$\Delta\boldsymbol{\theta} = \mathbf{J}^{-1}\,\mathbf{g}, \tag{18}$$

where $\mathbf{g}$ denotes the gradient of the negative log-likelihood cost function, and $\mathbf{J}$ is a Gauss–Newton approximation of the associated Hessian,

$$\mathbf{J} = \sum_{k=0}^{N-1} \left(\frac{\partial \mathbf{y}(k)}{\partial \boldsymbol{\theta}}\right)^{T} \mathbf{R}^{-1} \left(\frac{\partial \mathbf{y}(k)}{\partial \boldsymbol{\theta}}\right) \tag{19}$$

where $\mathbf{y}(k)$ denotes the model output vector and $\mathbf{R}$ the measurement noise covariance matrix.

In the maximum-likelihood formulation implemented in DLR's FITLAB toolbox for MATLAB [54], $\mathbf{J}$ represents an estimate of the Fisher information matrix [53, Chap. 4.XVII]. The parameter covariance is estimated as $\mathbf{P} = \mathbf{J}^{-1}$ and reported uncertainties correspond to standard deviation estimates $\sigma(\theta_i) = \sqrt{P_{ii}}$. The uncertainty estimates assume independent and identically distributed (IID) residuals; in closed-loop identification residuals are often correlated, so the reported values reflect the precision around a local optimum and may underestimate the true uncertainty, particularly in the presence of model mismatch and unmodeled dynamics. Since Gauss–Newton is a local method, the solution is highly sensitive to initialisation and can easily fall into nonphysical local optima; to mitigate this, parameters in this study were initialised using a combination of equation-error estimates and previously identified models [17].

6.0 Results

The results section first quantifies the measured differences between the clean and iced datasets using reconstructed aerodynamic coefficients, and then assesses how well the identified models reproduce these trends, including the implied changes in stability and damping.

6.1 Observed aerodynamic changes in the flight data

A comparative overview of the aerodynamic coefficients reconstructed from the clean and iced experiments according to Equation (4) is shown in Figure 8. The excitation manoeuvres drive the UAV through rapid, high-amplitude attitude changes spanning both positive and negative angles of attack, which enables a direct clean–iced comparison over a broader longitudinal envelope than is typically available in manned-aircraft icing datasets.

The reconstructed longitudinal coefficients exhibit several distinct features. Notably, the iced configuration shows a clear increase in drag, especially at higher angles of attack. Furthermore, the lift and drag profiles display an asymmetry around $\alpha \approx 0^{\circ}$ that suggests an aerodynamic regime change, while the iced pitching-moment exhibits a noticeably flatter slope at small angles of attack. In contrast, no corresponding asymmetry is evident in the lateral coefficients, consistent with the lateral model being kept symmetric.

6.2 Static lift–drag characteristics and break-point behaviour

To visualise the identified longitudinal behaviour without measurement noise and manoeuvre transients, Figure 9 shows the static lift curve, lift–drag curve and lift-to-drag ratio for the clean and iced models evaluated without any control surface deflection ($\delta_e = 0^{\circ}$) and pitch rate ($q = 0$ rad/s). The break-point formulation yields two smoothly blended regimes. As demonstrated in the lift coefficient plot, the lift generation is only slightly degraded by the ice accretion, showing a minor reduction in lift slope primarily

Downloaded from https://www.cambridge.org/core. 28 Sep 2026 at 04:58:16, subject to the Cambridge Core terms of use.

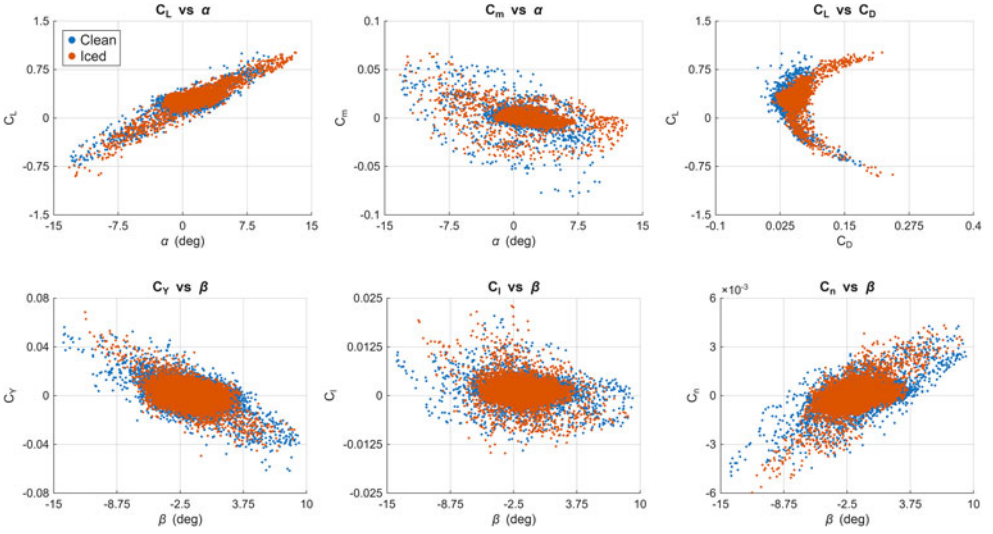

Figure 8. *Comparison of the aerodynamic coefficients reconstructed from the clean and iced configuration experiments. The shown data includes both the training and validation sets.*

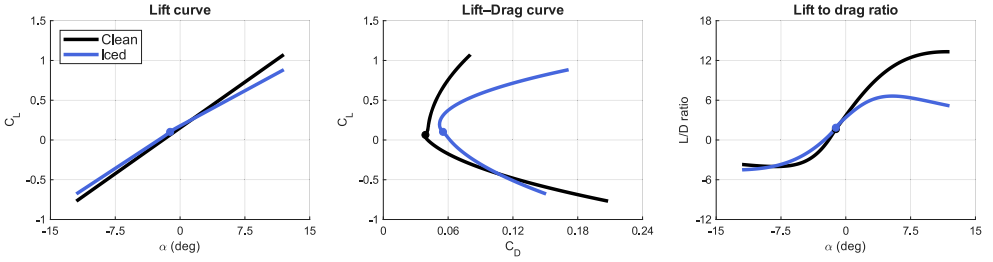

Figure 9. *Identified static lift and drag model curves evaluated at* $\delta_e = q = 0$*. The break-points at* $\alpha_0 = -0.02$ rad *are indicated by the filled dots.*

at positive angles of attack. Instead, the most dominant aerodynamic penalty is the increase in drag. The iced lift–drag curve is shifted to higher C_D values across most of the flight envelope. This substantial drag increase at positive angles of attack significantly degrades the aircraft's aerodynamic efficiency, roughly halving the maximum lift-to-drag ratio compared to the clean aircraft.

6.3 Model adequacy

The correspondence between the reconstructed coefficient measurements and the model outputs on the validation set (Table 6) is visually assessed in Figures 10 and 11. To quantitatively define model adequacy and evaluate the quality of the fit, statistical properties of the aerodynamic residuals – specifically the mean (μ), standard deviation (σ), and skewness – are presented in Table 10. A model is considered highly accurate if it can reproduce the measurements with minimal residuals, both in the measured outputs and the model parameters (output error and equation error).

Across both configurations, the lateral coefficients have very small remaining errors, indicated by the presented mean μ, standard deviation σ and skewness. It is also noteworthy that the statistical values for the clean and iced configurations are highly comparable in magnitude and sign for the lateral aerodynamic coefficients, further indicating that the model structure is well chosen to represent the aircraft's lateral aerodynamics.

Downloaded from https://www.cambridge.org/core. 28 Sep 2026 at 04:58:16, subject to the Cambridge Core terms of use.

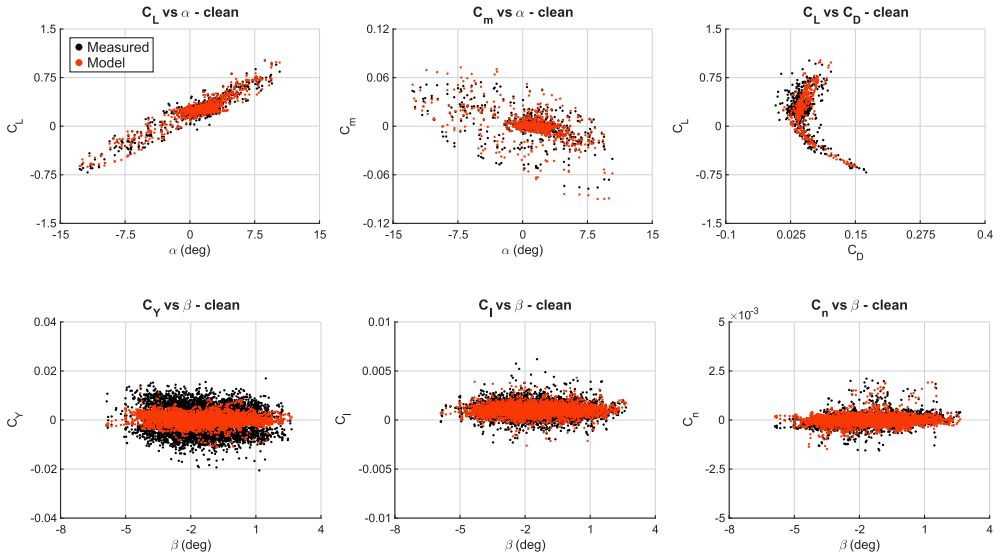

Figure 10. *Validation-set measurements and model outputs for the clean configuration.*

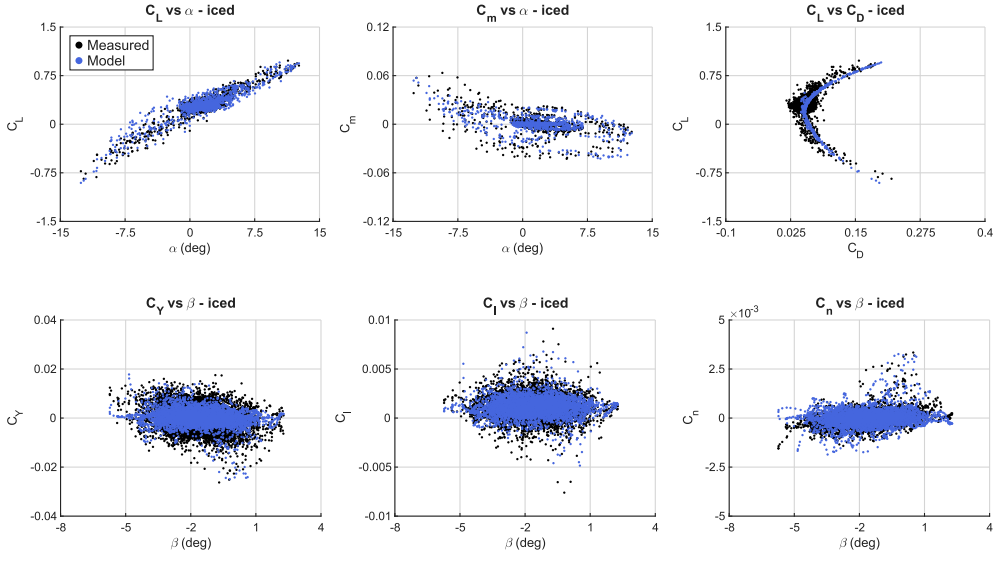

Figure 11. *Validation-set measurements and model outputs for the iced configuration.*

For the longitudinal aerodynamics, the residual statistics also indicate a good model fit, although with larger values than for the lateral axes. Visually, the clean model closely matches the reconstructed coefficient trends, accurately reproducing both the lift slope $C_L(\alpha)$ and the C_L–C_D curve. However, the mean error and standard deviation in the lift and drag coefficients are slightly higher than for the remaining coefficients. These longitudinal coefficients are inherently more challenging to accurately identify due to aero-propulsive coupling. Because the current identification method relies on the analytical cancellation of propulsion forces and moments to isolate the pure aerodynamic terms, any unmodeled thrust interactions directly propagate into the C_L and C_D residuals.

Downloaded from https://www.cambridge.org/core. 28 Sep 2026 at 04:58:16, subject to the Cambridge Core terms of use.

Table 10. *Statistical properties of the longitudinal and lateral aerodynamic model residuals*

	Clean			Iced		
	μ	σ	Skewness	μ	σ	Skewness
C_L	3.14×10^{-3}	2.85×10^{-2}	−0.30	4.75×10^{-3}	4.52×10^{-2}	−1.15
C_D	-1.91×10^{-3}	7.10×10^{-3}	−0.23	-4.33×10^{-3}	9.12×10^{-3}	−0.17
C_m	8.08×10^{-6}	2.55×10^{-3}	−1.28	-6.29×10^{-5}	2.78×10^{-3}	−0.06
C_Y	4.27×10^{-5}	7.30×10^{-3}	0.09	-1.41×10^{-4}	5.89×10^{-3}	0.05
C_l	4.54×10^{-5}	1.12×10^{-3}	0.42	3.05×10^{-5}	1.18×10^{-3}	0.66
C_n	-4.53×10^{-6}	4.26×10^{-4}	−0.19	-4.56×10^{-6}	4.11×10^{-4}	−0.12

Focusing on the iced configuration, the agreement is visibly weaker, and the predicted coefficient spread becomes narrower (C_L vs C_D in Figure 11). The large skewness for the iced lift coefficient indicates some remaining model deficiencies, suggesting that complex flow disruptions from the ice shapes likely exacerbate the propulsive coupling. Compounding this, the given aircraft, with its specific configuration (flying wing) and the complex aerodynamics of ice on the leading edge, poses significant challenges for model development, as already discussed. Despite these obstacles, the overall modelling approach (model structure and identified parameters) successfully captures the aircraft's aerodynamics. Consequently, the overall fit and model match are considered very good, as supported by the cross plots in Figures 10 and 11 and the time-domain reconstructions presented later in Figure 12.

6.3.1 Time-domain reconstruction

Selected time-domain reconstructions are shown in Figure 12. Overall, the models reproduce the manoeuvre responses well: the dominant acceleration and attitude trends are captured, and the simulations remain phase-consistent through the main excitation and subsequent settling. Minor differences in the realised elevator input are expected, because the manoeuvres are executed under stabilising feedback and the control surfaces reflect the closed-loop response of the autopilot rather than the pure manoeuvre commands, as detailed in subsection 5.2.

For the longitudinal case (Figure 12a and b), the clean model provides a close match across the measured outputs. It is noteworthy that these manoeuvres excite large angle-of-attack excursions, reaching approximately $\pm10^\circ$ in the clean configuration and exceeding $\pm10^\circ$ in the iced case. While such amplitudes approach the boundaries of the linear aerodynamic regime, similar excursions are not uncommon for small UAVs, as corroborated by 5-hole pitot flight measurements in Ref. [55]. Furthermore, higher-order lift terms were explicitly evaluated during the stepwise regression but did not meaningfully improve the model.

Turning to the iced reconstruction, the model remains qualitatively correct but exhibits reduced fidelity; in particular, the pitch rate, pitch angle and airspeed are not captured as tightly. Notably, the iced model takes longer to settle and shows a less sharp initial pitching reaction. Overall, the behaviour during the elevator manoeuvre indicates that the iced UAV configuration has slower pitch dynamics, consistent with a reduction in short-period frequency; this interpretation is supported by the eigenvalue analysis presented later in subsection 6.5.

For the lateral *1-2-1* manoeuvres (Figure 12c and d), the clean and iced time-domain responses are visually very similar. Both models reproduce the measured roll- and yaw-rate dynamics well, and the overall reconstruction quality is comparable across configurations. The most noticeable difference is a slightly reduced lateral-acceleration response in the iced case, suggesting a modest reduction in the effective side-force generated for a comparable lateral excitation. Beyond this, any icing-induced changes in lateral dynamics are subtle in the raw time histories for this manoeuvre class. Further insight is provided by the subsequent mode analysis, which shows that the roll and Dutch-roll modes shift toward slower dynamics even though the time-domain differences remain difficult to isolate by visual inspection alone.

Downloaded from https://www.cambridge.org/core. 28 Sep 2026 at 04:58:16, subject to the Cambridge Core terms of use.

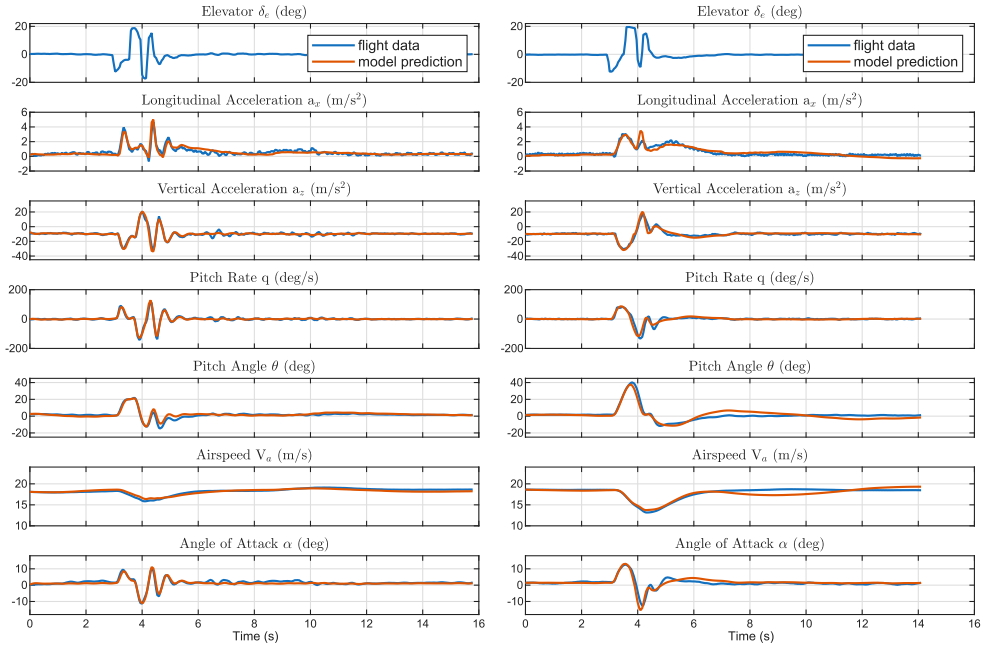

(a) Longitudinal *3-2-1-1* clean

(b) Longitudinal *3-2-1-1* iced

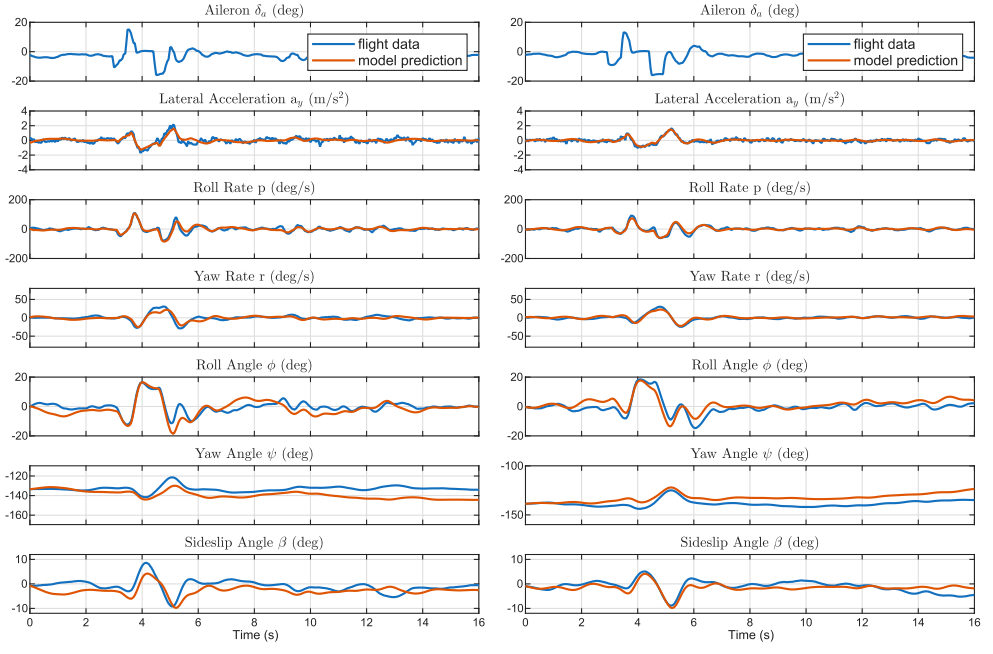

(c) Lateral *1-2-1* clean

(d) Lateral *1-2-1* iced

Figure 12. *Selected time-domain reconstruction comparison for clean and iced configurations.*

6.4 Identified coefficients

The numerical values and uncertainties of the identified coefficients are reported in Tables 11 and 12, with a visual summary provided in Figure 13. The uncertainties, computed as described in subsection 5.5, reflect the relative precision of the estimates: lateral model derivatives generally converge with

Downloaded from https://www.cambridge.org/core. 28 Sep 2026 at 04:58:16, subject to the Cambridge Core terms of use.

Table 11. *Identified coefficients of the nonlinear longitudinal aerodynamic model Eq. (15) for clean and iced configurations at 18 m/s*

Param.	Clean	StdDev. (Rel.%)	Iced	StdDev. (Rel.%)	$\boldsymbol{C}_{\text{iced/clean}}$ **(Δ %)**
C_{L0}	0.1523	0.0005 (0.3)	0.1775	0.0005 (0.3)	1.16 (+16)
$C_{L\alpha}$	4.3993	0.0201 (0.5)	3.3730	0.0159 (0.5)	0.77 (−23)
$C^{-}_{L\alpha}$	4.3993	0.0201 (0.5)	4.0862	0.0343 (0.8)	0.93 (−7)
C_{Lq}	0.4440	0.1364 (30.7)	0.2782	0.1208 (43.4)	0.63 (−37)
$C_{L\delta_e}$	0.5011	0.0123 (2.4)	0.3329	0.0169 (5.1)	0.66 (−34)
$C^{-}_{L\delta_e}$	0.5011	0.0123 (2.4)	1.5914	0.0357 (2.2)	3.18 (+218)
C_{D0}	0.0411	0.0005 (1.2)	0.0616	0.0008 (1.2)	1.50 (+50)
C_{Dq}	1.4793	0.0324 (2.2)	0.3457	0.0444 (12.8)	0.23 (−77)
C^{-}_{Dq}	0.6191	0.0351 (5.7)	0.3457	0.0444 (12.8)	0.56 (−44)
C_{Dk1}	−0.0032	0.0028 (86.4)	−0.0982	0.0037 (3.8)	30.82 (+2982)
C^{-}_{Dk1}	−0.0760	0.0054 (7.1)	−0.0627	0.0039 (6.3)	0.83 (−17)
C_{Dk2}	0.0373	0.0034 (9.0)	0.2518	0.0043 (1.7)	6.76 (+576)
C^{-}_{Dk2}	0.1835	0.0107 (5.8)	0.1010	0.0071 (7.1)	0.55 (−45)
C_{m0}	0.0067	0.0000 (0.4)	0.0010	0.0000 (1.3)	0.15 (−85)
$C_{m\alpha}$	−0.3307	0.0010 (0.3)	−0.0557	0.0004 (0.7)	0.17 (−83)
$C^{-}_{m\alpha}$	−0.3307	0.0010 (0.3)	−0.1804	0.0014 (0.8)	0.55 (−45)
C_{mq}	−0.8042	0.0108 (1.3)	−0.1575	0.0041 (2.6)	0.20 (−80)
$C_{m\delta_e}$	−0.2316	0.0008 (0.4)	−0.1004	0.0005 (0.5)	0.43 (−57)
$C^{-}_{m\delta_e}$	−0.2316	0.0008 (0.4)	−0.1323	0.0013 (1.0)	0.57 (−43)

Table 12. *Identified coefficients of the lateral aerodynamic model Eq. (16) for clean and iced configurations at 18 m/s*

Param.	Clean	StdDev. (Rel.%)	Iced	StdDev. (Rel.%)	$\boldsymbol{C}_{\text{iced/clean}}$ **(Δ %)**
C_{Y0}	−0.0085	0.0002 (2.2)	−0.0057	0.0002 (2.7)	0.66 (−34)
$C_{Y\beta}$	−0.2700	0.0028 (1.0)	−0.2695	0.0036 (1.3)	1.00 (00)
C_{Yp}	−0.1920	0.0112 (5.9)	−0.0626	0.0104 (16.7)	0.33 (−67)
C_{Yr}	0.5389	0.0162 (3.0)	0.4412	0.0194 (4.4)	0.82 (−18)
$C_{Y\delta_a}$	0.0832	0.0034 (4.0)	0.0523	0.0024 (4.6)	0.63 (−37)
C_{l0}	0.0016	0.0000 (1.6)	0.0014	0.0000 (2.2)	0.91 (−9)
$C_{l\beta}$	−0.0644	0.0005 (0.8)	−0.0745	0.0008 (1.1)	1.16 (+16)
C_{lp}	−0.2124	0.0023 (1.1)	−0.1746	0.0026 (1.5)	0.82 (−18)
C_{lr}	0.1135	0.0026 (2.3)	0.1057	0.0051 (4.8)	0.93 (−7)
$C_{l\delta_a}$	0.0865	0.0007 (0.8)	0.0617	0.0005 (0.8)	0.71 (−29)
C_{n0}	0.0007	0.0000 (1.0)	0.0006	0.0000 (1.8)	0.82 (−18)
$C_{n\beta}$	0.0198	0.0001 (0.6)	0.0247	0.0003 (1.2)	1.25 (+25)
C_{np}	−0.0204	0.0007 (3.2)	−0.0162	0.0009 (5.6)	0.79 (−21)
C_{nr}	−0.1069	0.0010 (0.9)	−0.0741	0.0014 (1.9)	0.69 (-31)
$C_{n\delta_a}$	−0.0043	0.0002 (4.5)	−0.0050	0.0002 (3.5)	1.17 (+17)

lower relative uncertainty than the longitudinal, consistent with the reduced longitudinal time-domain fidelity observed in the iced case.

Overall, the estimated changes agree with the trends already visible in the reconstructed coefficients and with the subsequent mode analysis. In the longitudinal model, icing primarily manifests as a drag penalty, reflected by a 50% increase in zero-lift drag (C_{D0}) and a substantially larger lift-dependent drag curvature (C_{Dk2}), together with a reduced lift-curve slope in the main ($\alpha > 0$) regime ($C_{L\alpha}$: −23%).

Downloaded from https://www.cambridge.org/core. 28 Sep 2026 at 04:58:16, subject to the Cambridge Core terms of use.

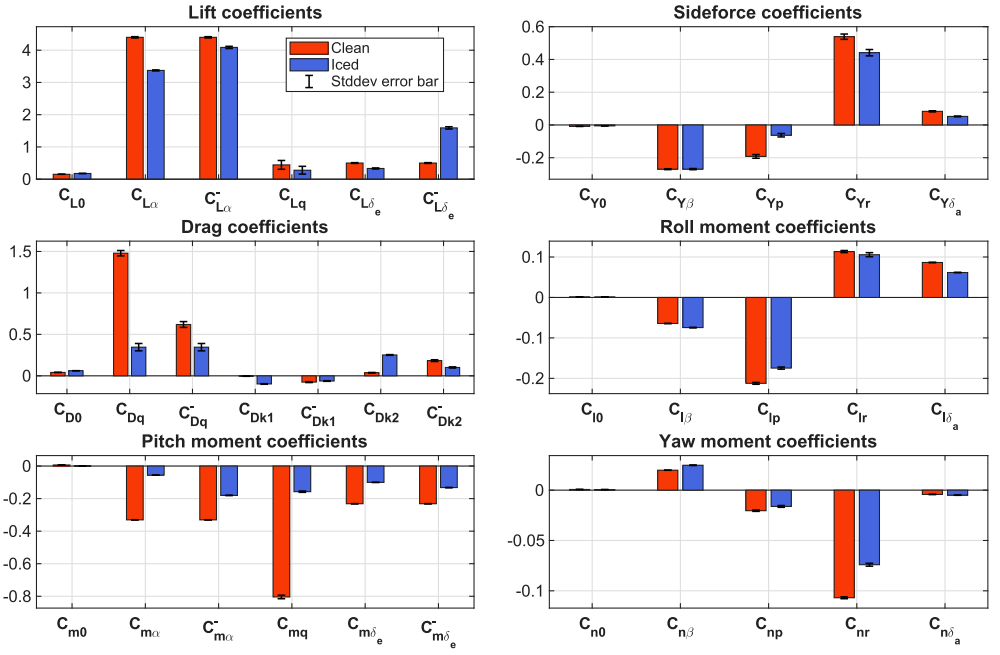

Figure 13. *Visual comparison of the identified coefficients.*

Percent changes for coefficients with near-zero clean values should be interpreted with caution. Most notably, the clean C_{Dk1} term exhibits a high relative uncertainty (86.4%), rendering it statistically indistinguishable from zero and arguably unnecessary for the clean baseline structure, albeit retained here for comparison purposes. Because this baseline value is effectively zero, the calculated relative change for the iced configuration (+2982%) is mathematically inflated. Consequently, the total change in drag presented in Figure 9 provides a more robust comparison between the clean and iced models. Turning to the lift behaviour in the negative angle-of-attack regime, the slope ($C_{L\alpha}^{-}$) changes only modestly compared to the primary regime.

Furthermore, the strong reductions in effective pitch stiffness ($C_{m\alpha}$: −83%) and pitch-rate damping (C_{mq}: −80 %) provide a direct parametric explanation for the slower longitudinal behaviour observed in the iced time histories. Crucially, the collapse in $C_{m\alpha}$ indicates a significant degradation of the aircraft's longitudinal static stability. Recalling Equation (3), the dimensionless static margin ($-C_{m\alpha}/C_{L\alpha}$) drops from 7.5% in the clean configuration to 1.7% in the iced case. Due to the simplifying AC and CG assumptions, and the model uncertainty around the iced pitch dynamics, these values should not be interpreted in absolute terms; however, the overall trend is clear: the static stability margin is significantly reduced in the iced case. In the lateral model, the aerodynamic changes are generally smaller. In particular, $C_{Y\beta}$ remains unchanged, which is consistent with the fact that the winglets and fuselage were not modified.

6.5 Linearized dynamics

To connect the identified aerodynamic changes to classical handling-quality metrics, the clean and iced nonlinear models were trimmed and linearised at the same nominal condition (level flight at $V_a = 18$ m/s, zero wind). The resulting pole locations are shown in Figure 14 and summarised in Table 13. Mode-based comparisons are widely used in the icing literature as they provide a compact description of how stability and response characteristics change with configuration [15, 16].

Downloaded from https://www.cambridge.org/core. 28 Sep 2026 at 04:58:16, subject to the Cambridge Core terms of use.

Table 13. *Clean and iced poles trimmed at ($V_a = 18$ m/s, level flight, no wind)*

Clean trim: $V_a^\star = 18$ m/s, $\alpha^\star = 1.26°$, $\delta_e^\star = -0.14°$, $\Omega_p^\star = 508$ rad/s, $T^\star = 6.3$ N
Iced trim: $V_a^\star = 18$ m/s, $\alpha^\star = 1.69°$, $\delta_e^\star = -0.39°$, $\Omega_p^\star = 562$ rad/s, $T^\star = 7.9$ N

Mode	Pole		Damping	Frequency (rad/s)	Time constant (s)
Longitudinal modes					
Phugoid	Clean:	$-0.22 \pm 0.64i$	0.32	0.68	4.63
	Iced:	$-0.16 \pm 0.60i$	0.25	0.62	6.34
Short-period	Clean:	$-8.58 \pm 10.72i$	0.63	13.73	0.12
	Iced:	$-4.83 \pm 4.79i$	0.71	6.80	0.21
Lateral modes					
Spiral	Clean:	-0.43	1.00	0.43	2.34
	Iced:	-0.24	1.00	0.24	4.13
Dutch-roll	Clean:	$-2.19 \pm 4.03i$	0.48	4.59	0.46
	Iced:	$-0.84 \pm 4.23i$	0.19	4.32	1.19
Roll	Clean:	-11.79	1.00	11.79	0.08
	Iced:	-7.47	1.00	7.47	0.13

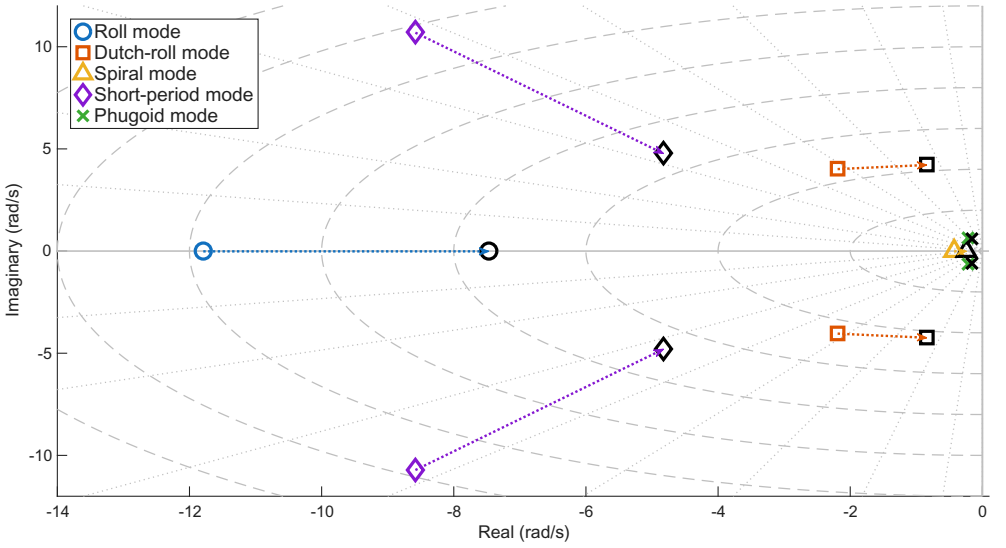

Figure 14. *Pole plot showing the aerodynamic modes of the linearised Skywalker X8 dynamics in clean (colored) and iced (black) configurations.*

In the longitudinal dynamics, the phugoid mode shifts slightly towards the origin in the iced case. This contrasts with the reported trend that wing-ice drag penalties move the phugoid roots away from the origin, indicating increased damping, through a reduced L/D ratio [15]. The latter decreases from 5.81 (clean case) to 5.12 (iced case), which would be basically in line with the findings in Ref. [15]. Nevertheless, there are three UAV-specific artefacts likely contributing to the found disagreement. First, the added ice mass is non-negligible (+11%), which shifts the trim, given in Table 13, to a higher angle-of-attack and thus a higher L/D than if the mass change was negligible. Second, because the iced coefficients are normalised by the *clean* reference geometry, any effective increase in lifting planform manifests as a larger trimmed lift coefficient $C_L^\star$, which mathematically reduces the ratio $C_D^\star/C_L^\star$ and thus reduces the predicted phugoid damping. The classical phugoid mode approximation [56, Chap. 6]

Downloaded from https://www.cambridge.org/core. 28 Sep 2026 at 04:58:16, subject to the Cambridge Core terms of use.

reveals this fundamental relation between the damping ratio ζ_{ph} and the trim L/D ratio when thrust-velocity coupling is neglected:

$$\omega_{ph} \approx \sqrt{2}\frac{g}{u^\star}, \qquad \zeta_{ph} \approx \frac{C_D^\star}{C_L^\star} \tag{20}$$

However, a more complete approximation from the same text demonstrates that phugoid damping is strictly governed by the dimensional speed-damping derivative X_u:

$$\zeta_{ph} \approx \frac{-X_u/m}{2}\sqrt{\frac{u^\star}{-gZ_u/m}} \quad \text{where} \quad X_u = \left(\frac{\partial T}{\partial u} - \frac{\partial D}{\partial u}\right) \tag{21}$$

The third UAV-specific artefact directly alters this speed-damping term. Because the pusher propeller operates within the turbulent wake of the iced wings as detailed in subsection 4.2, the thrust-velocity coupling ($\partial T/\partial u$) is reduced. This degradation is directly observable when linearising the identified models at trim: (X_u/m) decreases in magnitude from $-0.44\,\mathrm{s}^{-1}$ in the clean to $-0.39\,\mathrm{s}^{-1}$ in the iced configuration, while the mass-normalised heave-damping (Z_u/m) changes from $-0.60\,\mathrm{s}^{-1}$ to $-0.66\,\mathrm{s}^{-1}$. Evaluating the approximation in Equation (21) with these parameters predicts a phugoid damping *reduction* from 0.38 in the clean case to 0.33 in the iced case, which mirrors the trend of the full linearised poles (going from 0.32 to 0.25) reported in Table 13. Thus, this complex aero-propulsive interaction decouples the phugoid damping from pure aerodynamic drag, providing a mathematically consistent explanation for the observed reduction in damping.

In contrast, the short-period mode exhibits the largest longitudinal change: the oscillation frequency decreases markedly and the real part moves closer to the origin. This is consistent with the time-domain reconstructions, where the iced response in the fastest part of the manoeuvre is visibly slower. The identified reductions in effective pitch stiffness $C_{m\alpha}$ and pitch-rate damping C_{mq} corroborate the slower short-period response, which is also consistent with wing-ice observations in manned-aircraft studies reporting frequency reductions under leading-edge ice accretion [15]. In the lateral dynamics, the roll and Dutch-roll poles move toward the origin, indicating reduced roll damping. This is consistent with the reductions in roll- and yaw-rate damping derivatives identified in Table 12, as well as the considerable increase in moments of inertia about the roll and yaw axes (detailed in section 3). The spiral mode becomes less stable as well at this trim point; both stabilisation and destabilisation under wing ice are reported in the literature, reflecting the mode's sensitivity to complex roll–yaw coupling rather than a single dominant derivative [15, 16].

6.6 Steady-state power balance

To validate the operational utility of the identified aerodynamic models, a steady-state energy balance was evaluated. By isolating the mechanical aerodynamic power from the coupled electrical powertrain, the fidelity of the identified drag penalty can be assessed against the measured battery power.

The theoretical aerodynamic drag power predicted by the identified static models ($P_{D,\mathrm{model}}$) and the equivalent measured drag power derived from the battery ($P_{D,\mathrm{batt}}$) are defined as:

$$P_{D,\mathrm{model}} = \bar{q}SC_DV_a \tag{22}$$

$$P_{D,\mathrm{batt}} = P_{\mathrm{batt}}\,\eta_{\mathrm{prop}} \tag{23}$$

Using the established apparent overall propulsive efficiency baseline ($\eta_{\mathrm{prop}} = 0.6454$) in subsection 4.2, the measured electrical battery power was scaled to its equivalent aerodynamic drag power. This was compared to the model predictions evaluated at the trim conditions outlined in Table 13. The resulting longitudinal power balance is summarised in Table 14.

Overall, the steady-state power balance demonstrates close agreement with flight data. The models predict the required electrical battery power with relative errors of -0.8% and $+7.6\%$ for the clean and iced configurations, respectively. The resulting over-prediction of the battery power penalty (45.5 W modelled vs. 28.4 W measured) could be a consequence of the efficiency anchoring assumption.

Downloaded from https://www.cambridge.org/core. 28 Sep 2026 at 04:58:16, subject to the Cambridge Core terms of use.

Table 14. *Steady-state power balance at nominal trim ($V_a = 18\,m/s$)*

	Aerodynamic drag power		Electrical battery power	
Configuration	Measured	Modeled (Error)	Measured	Modeled (Error)
Clean flight	113.9 W	113.0 W (−0.8%)	176.6 W	175.1 W (−0.8%)
Iced flight	132.3 W	142.4 W (+7.6%)	205.0 W	220.6 W (+7.6%)

Note: Modeled values use identified aerodynamic coefficients anchored to the clean apparent efficiency (subsection 4.2). Percentages show relative error against measured flight data.

By forcing propulsive efficiency to remain constant across both configurations, any unmodelled propeller efficiency degradation would be absorbed into the aerodynamic drag. While decoupling these effects would require wind-tunnel tests of the UAV-mounted propeller, this lumped-parameter approach safely bounds the operational penalty, yielding a conservative endurance model suitable for icing-aware flight operations.

7.0 Discussion

7.1 Pilot observations

During the iced flights the pilot indicated a less responsive aircraft with reduced sensitivity to gusts. Moreover, in the landing phase the aircraft required a higher angle-of-attack, making touchdown handling more demanding. These qualitative observations are consistent with the identified increase in drag, reduced lift and reduced control surface effectiveness.

7.2 Relation to literature on aircraft icing

Overall, the identified coefficient changes are qualitatively consistent with the other reported aerodynamic signatures of wing leading-edge icing: a pronounced drag penalty, a reduced effective lift-curve slope in the operational α range and degraded control effectiveness. For example, the presented increase in zero-lift drag (C_{D0}) of 50% is of the same order as the 60% increase reported in Ref. [11] for the NASA DHC-6 Twin Otter aircraft, which was measured following a 45-minute natural icing encounter at 67.4 m/s airspeed (LWC = 0.20 g/m^3, MVD = 15 μm, at −5.3 °C). Similar large drag increases are also reported in system-identification-based studies of an Embraer light business jet equipped with artificial leading-edge ice, including isolated wing zero-lift drag penalties exceeding 70% [12]. These comparisons support that the ice-induced drag degradation inferred for the present UAV is not atypical in order of magnitude, even though the airframe scale and Reynolds number differ.

The reduction in lift-curve slope in the primary regime ($C_{L\alpha}$: −23%) aligns with the expected degradation of lifting performance under leading-edge ice, but the magnitude is larger than the −8% reported for the natural icing encounter in Ref. [11]. This larger sensitivity is plausible for a small fixed-wing UAV because leading-edge roughness and separation-bubble formation can have a more disproportionate effect at low Reynolds numbers [57], and because the present accretion severity is intentionally pronounced. Consistent with this interpretation, leading-edge ice in Ref. [12] is specifically associated with stronger lift-curve degradation of −15% in the higher-α regime.

The pitching-moment and control derivatives indicate a substantial loss of longitudinal stiffness and pitch-rate damping: $C_{m\alpha}$ and C_{mq} decrease in magnitude by about 83% and 80%, respectively, while elevator effectiveness $C_{m\delta_e}$ decreases by about 57%. The direction of these changes is consistent with reduced static stability and damping, and provides a direct mechanism for the observed short-period mode shift. However, the magnitude is considerably larger than typical derivative changes reported in some full-scale benchmarks (e.g. 10% reduction in $C_{m\alpha}$ in Ref. [11]). Although this is the most direct quantitative comparison available, the discrepancy is expected since the Twin Otter benchmark evaluated simulated glaze ice isolated to the tail surfaces. Furthermore, for the presented closed-loop UAV

Downloaded from https://www.cambridge.org/core. 28 Sep 2026 at 04:58:16, subject to the Cambridge Core terms of use.

identification with a quasi-steady aerodynamic structure, part of the icing-induced unmodeled dynamics can be absorbed into the apparent moment derivatives. This motivates treating the modal consequences related to pitch dynamics (short-period slowdown) as the most robust dynamic implication, instead of focusing on the individual coefficients.

Compared to the significant degradation observed in the longitudinal dynamics, the changes in the lateral-directional coefficients are generally much smaller. In particular, the unchanged $C_{Y\beta}$ is consistent with the fact that the primary vertical surfaces were not directly modified by the applied wing-leading-edge ice. At the same time, a systematic reduction is observed across all roll- and yaw-rate derivatives (C_{lp}, C_{lr}, C_{np}, C_{nr}, C_{Yp}, C_{Yr}). This uniform loss of rotational damping and cross-coupling effectiveness, combined with the increased rotational inertia of the iced wings, provides the parametric basis for the observed slower roll and Dutch-roll modes. The combination of small visible differences in time-series responses but measurable changes in modal properties makes the lateral dynamics inherently harder to analyse from raw flight data alone. As noted in Ref. [12], lateral changes are generally reported to be much more configuration- and geometry-dependent than the universally dominant, drag-driven longitudinal trends.

7.3 Unsteady aerodynamic effects

Unsteady stall identification studies have shown that once separation occurs, aerodynamic forces and moments cannot be represented as functions of angle-of-attack alone, but require internal states to capture delayed separation, hysteresis and load overshoot [58]. Modern unsteady aerodynamics further emphasises that separated flows exhibit phase lag, memory effects and vortex shedding, which may introduce oscillatory loads even at nearly constant kinematic conditions [59]. Under severe icing, these mechanisms can become dominant because ice-induced roughness and leading-edge shape changes promote earlier separation and stronger history dependence (hysteresis/lag). Consistent with this, the lower fidelity of the iced longitudinal reconstructions compared to the clean case suggests that the icing-induced dynamics are not fully represented by a quasi-steady coefficient map in (α, q^*, δ_e).

A possible extension of the present framework is to augment the longitudinal model with an unsteady component, e.g. an internal separation state with first-order lag driven by angle-of-attack or potentially normalised pitch rate (q^*), which can represent load delay without requiring an explicit angle-of-attack time derivative ($\dot{\alpha}$) in the measurement model. Such dynamic augmentations are closely aligned with Δ-model concepts used for iced-aircraft identification, where additional terms are introduced to capture configuration-dependent, non-quasi-steady behaviour when static maps are insufficient [12]. More detailed extensions (e.g. hysteresis loops or multiple wake/vortex states) are possible but would likely require improved air-data instrumentation to remain identifiable from flight data.

8.0 Conclusion

This study provides quantitative answers to the three defined research questions:

RQ1: *How does wing icing alter the aerodynamics of a small fixed-wing UAV?*

Wing icing produced a clear aerodynamic degradation dominated by a substantial drag penalty that roughly halved the maximum lift-to-drag ratio, alongside a reduced lift-curve slope in the primary regime ($\alpha > 0$). Longitudinally, the identified reductions in effective pitch stiffness ($C_{m\alpha}$) and pitch-rate damping (C_{mq}) led to a significantly reduced static stability margin and slower short-period pitch dynamics. This was further compounded by reduced elevator effectiveness. In contrast, the lateral coefficients and time-domain reconstructions showed smaller changes, with the primary observed effect being a slower response in the linearised roll mode and reduced Dutch-roll damping.

RQ2: *Can quasi-steady models capture these icing-induced changes?*

Downloaded from https://www.cambridge.org/core. 28 Sep 2026 at 04:58:16, subject to the Cambridge Core terms of use.

A quasi-steady coefficient model with a minimal break-point structure captures the dominant static lift/drag trends and provides good time-domain reconstructions, with a higher fidelity in the clean case and reduced longitudinal fidelity in the iced case. The remaining discrepancies are most pronounced in pitching-moment-related channels, indicating that icing introduces additional unmodeled dynamics that are not fully represented within the adopted quasi-steady structure. For lateral dynamics, the quasi-steady model adequately represents the flight measurements without requiring structural modifications.

RQ3: *What are the implications for IPS/IDS and GNC of small fixed-wing UAVs?*

The identified parameter shifts and modal trends suggest actionable signatures and design drivers for icing-aware autonomy. For IDS, the most informative indicators are the drag-related changes and the consistent shift in short-period and lateral modal properties, which affect response rate and damping. For robust GNC and envelope protection, the results highlight the need to preserve stability margins under reduced longitudinal stiffness/damping (i.e. reduced $C_{m\alpha}$, C_{mq}) and slower roll response, e.g. via gain scheduling on estimated icing severity, setting conservative bandwidth targets and explicit monitoring of modal damping proxies. Furthermore, the mathematically closed aero-propulsive baseline scaling yields an accurate, slightly conservative systemic endurance model. This enables development of battery-aware return-to-home algorithms and path planning in icing conditions.

The major contributions of this paper are:

- An experimental system-identification study of leading-edge wing icing effects on a small fixed-wing UAV, using 3D-printed shapes representative of intentionally severe rime ice accretions generated in an IWT. The identified aerodynamic effects are explicitly compared and contextualised against established aircraft icing results from manned-aviation literature.
- Validation of the identified quasi-steady aerodynamic model against measured flight power consumption, yielding a conservative energy baseline capable of predicting realistic icing-induced power requirements.
- Identification and validation of clean and iced aerodynamic models, providing a quantitative baseline for future icing-aware flight control, detection systems and envelope protection for small UAVs operating in adverse weather.

8.1 Future work

Future work directions are: (i) simulation-based evaluation of clean/iced models in representative manoeuvres and development of transitional icing models for scenario studies, (ii) augmentation of the longitudinal model with minimal unsteady aerodynamics to better capture iced pitch dynamics and (iii) development of model-based icing detection and protection logic adapted to small fixed-wing UAVs.

Acknowledgements. The work is sponsored by the Research Council of Norway and Ubiq Aerospace AS through the projects 316425 and 350469. The authors thank the NTNU UAV Lab, especially Pål Kvaløy, Morten Einarsve and Dr. Kristoffer Gryte for their help with the setup of the UAV as well as organising and performing the flight experiments.

Data availability. The 106 flight experiments that support the findings of this study are available through the DataverseNO public repository [60].

Competing interests. The authors declare none.

Use of artificial intelligence. During the preparation of this work, the author(s) used Google Gemini 3.1 Pro to assist with language editing, phrasing refinement and readability improvements. After using this tool, the authors rigorously reviewed and edited the content and take full responsibility for the final manuscript.

Downloaded from https://www.cambridge.org/core. 28 Sep 2026 at 04:58:16, subject to the Cambridge Core terms of use.

References

[1] Federal Aviation Administration, Unmanned Aircraft Systems Beyond Visual Line of Sight Aviation Rulemaking Committee Final Report. Tech. rep. Accessed Mar 2026. Federal Aviation Administration, March 2022. https://www.faa.gov/regulations_policies/rulemaking/committees/documents/index.cfm/document/information/documentID/5424

[2] Zipline Team, The Wild, Wild Nest. Zipline International Inc. August 2024. https://www.zipline.com/newsroom/the-wild-wild-nest-cold-weather-drone (accessed on 05/27/2026).

[3] Tacconi, R., Marini, M.R., Saraceno, M., Foresti, G.L., Cinque, L. and Mecca, A. A comprehensive taxonomy of UAVs: a comparative feature matrix for hardware, capabilities, and payloads, *IEEE Access*, 2026, **14**, pp 3821–3851. https://doi.org/10.1109/ACCESS.2025.3642069

[4] Sørensen, K.L., Borup, K.T., Hann, R., Bernstein, B.C. and Pellicano, P. Icing Impact on UAS and AAM Operations in Selected US Metropolitan Areas. Tech. rep. (Accessed April 2026). UBIQ Aerospace, 2024. http://www.ubiqaerospace.com/climate-report

[5] Hansbø, M. and Hoelsæter, Ø. *Icing and wind - implications and mitigations in high-intensity, safety-critical drone operations in Norway*. FFI-RAPPORT 22/01459. Norwegian Defence Research Establishment (FFI), June 24, 2022.

[6] Hann, R. and Johansen, T.A., *Unsettled Topics in Unmanned Aerial Vehicle Icing*. Tech. rep. SAE Technical Paper, 2020. https://doi.org/10.4271/EPR2020008

[7] Cao, Y., Tan, W. and Wu, Z. Aircraft icing: an ongoing threat to aviation safety, *Aerosp. Sci. Technol.*, 2018, **75**, pp 353–385. https://doi.org/10.1016/j.ast.2017.12.028

[8] Jones, K.H. and Gross, J.N. Reducing Size, Weight, and Power (SWaP) of perception systems in small autonomous aerial systems, in *14th AIAA Aviation Technology, Integration, and Operations Conference*. https://doi.org/10.2514/6.2014-2705

[9] Løw-Hansen, B., Hann, R., Stovner, B.N. and Johansen, T.A. UAV icing: a survey of recent developments in ice detection methods, *IFAC-PapersOnLine*, 2023, **56**, pp 10727–10739. https://doi.org/10.1016/j.ifacol.2023.10.733

[10] Maio, L., Moore, J., Cook, D.E. and Potluri, P.A review of ice detection technologies, *Prog. Aerosp. Sci.*, 2026, **161**, p 101158. ISSN: 0376-0421. https://doi.org/10.1016/j.paerosci.2025.101158

[11] Bragg, M., Hutchison, T. and Merret, J. Effect of ice accretion on aircraft flight dynamics, in *38th Aerospace Sciences Meeting and Exhibit*. https://doi.org/10.2514/6.2000-360

[12] Deiler, C. Aerodynamic modeling, system identification, and analysis of iced aircraft configurations, *J. Aircr.*, 2018, **55**, pp 145–161. https://doi.org/10.2514/1.C034390

[13] Deiler, C. Flight characteristics with different supercooled large droplet ice configurations, *The Aeronaut. J.*, 2022, **126**, pp 848–865. https://doi.org/10.1017/aer.2021.98

[14] Broeren, A.P., Potapczuk, M.G., Lee, S., Woodard, B.S., Bragg, M.B. and Smith, T.G. Experimental aerodynamic simulation of glaze ice accretion on a swept wing, in *International Conference on Icing of Aircraft, Engines, and Structures*, June 2019. https://doi.org/10.4271/2019-01-1987

[15] Deiler, C. Flight Characteristics of Iced Aircraft, in *AIAA Scitech 2019 Forum*. https://doi.org/10.2514/6.2019-0560

[16] Cao, Y.H., Wu, Z.L. and Su, Y. Aircraft flight characteristics in icing conditions, *Prog. Aerosp. Sci.*, 2015, **74**, pp 62–80. ISSN: 0376-0421. https://doi.org/10.1016/j.paerosci.2014.12.001

[17] Løw-Hansen, B., Hann, R., Gryte, K., Johansen, T.A. and Deiler, C. Modeling and identification of a small fixed-wing UAV using estimated aerodynamic angles, *CEAS Aeronaut. J.*, 2025, **16**, pp 501–523. ISSN: 1869-5590. https://doi.org/10.1007/s13272-025-00816-3

[18] Longobardi, P. and Skaloud, J. Aerodynamic modeling of a delta-wing UAV for model-based navigation, *CEAS Aeronaut. J.*, 2024,**15**, pp 283–301. https://doi.org/10.1007/s13272-024-00727-9

[19] Hann, R., Hearst, R.J., Sætran, L.R. and Bracchi, T. Experimental and numerical icing penalties of an S826 airfoil at low Reynolds numbers, *Aerospace*, 2020, **7**. ISSN: 2226-4310. https://doi.org/10.3390/aerospace7040046

[20] Fajt, N., Hann, R., & Lutz, T. The influence of meteorological conditions on the icing performance penalties on a UAV airfoil, in *8th European Conference for Aeronautics and Space Sciences (EUCASS)*, 2019. https://doi.org/10.13009/EUCASS2019-240

[21] Lindner, M., Wallisch, J. and Hann, R., UAV icing: Numerical simulation of icing effects on wing and empennage, Tech. rep. SAE Technical Paper, 2023. https://doi.org/10.4271/2023-01-1384

[22] Han, N., et al. A flight-testing campaign to examine inflight icing characteristics and its effects on the flight performance of an unmanned-aerial-vehicle, in *Cold Regions Science and Technology 207*, 2023, p 103775. ISSN: 0165-232X. https://doi.org/10.1016/j.coldregions.2023.103775

[23] Liu, Y., Li, L., Chen, W., Tian, W. and Hu, H. An experimental study on the aerodynamic performance degradation of a UAS propeller model induced by ice accretion process, *Exp.Therm. Fluid Sci.*, 2019, **102**, pp 101–112. https://doi.org/10.1016/j.expthermflusci.2018.11.008

[24] Nilamdeen, S., Zhang, Y. and Ozcer, I., An ice shedding model for rotating components, *Tech. rep. SAE Technical Paper,* 2019. https://doi.org/10.4271/2019-01-2003

[25] Oswald, J.W., Enache, A., Hann, R. and Glabeke, G. UAV icing: experimental and numerical study of glaze ice performance penalties on an RG-15 airfoil, in *AIAA Scitech 2022 Forum*, 2022, p 1976. https://doi.org/10.2514/6.2022-1976

[26] Müller, N.C. and Hann, R., UAV Icing: 3D Simulations of Propeller Icing Effects and Anti-Icing Heat Loads, *Tech. rep. SAE Technical Paper*, 2023. https://doi.org/10.4271/2023-01-1383

[27] Muhammed, M., Harvey, D., Khawaja, H.A., Virk, M.S. and Momen, G. In-cloud ice accretion and performance degradation of UAV propellers in forward flight: an experimental study, *Cold Reg. Sci. Technol.*, 2025, **239**, p 104599. https://doi.org/10.1016/j.coldregions.2025.104599

Downloaded from https://www.cambridge.org/core. 28 Sep 2026 at 04:58:16, subject to the Cambridge Core terms of use.

[28] Løw-Hansen, B., Müller, N.C., Coates, E.M. and Johansen, T.A., Identification of an electric UAV propulsion system in icing conditions, *Tech. rep. SAE Technical Paper*, 2023. https://doi.org/10.4271/2023-01-1378
[29] Deiler, C. Testing of an indirect ice detection methodology in the Horizon 2020 project SENS4ICE, *CEAS Aeronaut. J.*, 2025, **16**, pp 213–229. https://doi.org/10.1007/s13272-024-00783-1
[30] Adelina Ghindaoanu, N., Gryte, K., Reinhardt, D. and Johansen, T.A. Control of fixed-wing UAVs in icing conditions using nonlinear model predictive control, in *2024 European Control Conference (ECC)*, 2024, pp 1461–1466. https://doi.org/10.23919/ECC64448.2024.10591240
[31] Högnadottir, S., Gryte, K. and Hann, R. Inner-loop control of fixed-wing unmanned aerial vehicles in icing conditions, in *AIAA Scitech 2023 Forum*, 2023. https://doi.org/10.2514/6.2023-1049
[32] Kleiven, R., Gryte, K. and Johansen, T.A. Robust and gain-scheduled flight control of fixed-wing UAVs in wind and icing conditions, in *2022 IEEE Aerospace Conference (AERO)*, 2022, pp 1–12. https://doi.org/10.1109/AERO53065.2022.9843837
[33] Tiihonen, M., Jokela, T. and Makkonen, L. VTT Icing wind tunnel 2.0. English, *Winterwind Presentations 2016. Winterwind International Wind Energy Conference; Conference date* 08-02-2016 Through 10-02-2016. February 2016.
[34] Borup, K.T., Fossen, T.I. and Johansen, T.A. A machine learning approach for estimating air data parameters of small fixed-wing UAVs using distributed pressure sensors, *IEEE Trans. Aerosp. Electron. Syst.*, 2019, **56**, pp 2157–2173. https://doi.org/10.1109/TAES.2019.2945383
[35] Hann, R., Müller, N. and Lindner, M., UAV icing: experimental validation data for predicting ice shapes at low Reynolds numbers, *Tech. rep. SAE Technical Paper*, 2023. https://doi.org/10.4271/2023-01-1372
[36] Jeck, R.K., Icing design envelopes (14 CFR Parts 25 and 29, Appendix C) converted to a distance-based format, *Tech. rep. FAA technical center Atlanta City NJ,* 2002.
[37] Macklin, W.C. The density and structure of ice formed by accretion, *Quart. J. R. Meteorol. Soc.*, 1962, **88**, pp 30–50. https://doi.org/10.1002/qj.49708837504
[38] Camello, S., Lee, S., Lum, C. and Bragg, M.B. Generation of full-span leading-edge 3D ice shapes for swept-wing aerodynamic testing, in *8th AIAA Atmospheric and Space Environments Conference. AIAA*, 2016. https://doi.org/10.2514/6.2016-3737
[39] Potapczuk, M.G. and Broeren, A.P. An integrated approach to swept wing icing simulation, in *2017 European Conference for Aeronautics and Space Sciences (EUCASS)*, 2017. https://doi.org/10.13009/EUCASS2017-687
[40] Fujiwara, G.E.C. and Bragg, M.B. Method for designing three-dimensional swept hybrid wings for icing wind-tunnel tests, *J. Aircr.*, 2019, **56**, pp 730–746. https://doi.org/10.2514/1.C035136
[41] Jardin, M.R. and Mueller, E.R. Optimized measurements of UAV mass moment of inertia with a bifilar pendulum, in *Collection of Technical Papers - AIAA Guidance, Navigation, and Control Conference 2007 5*, 2007, pp 4790–4812. https://doi.org/10.2514/6.2007-6822
[42] Anderson, J.D.Jr, *Fundamentals of Aerodynamics, 6th ed*, McGraw-Hill Education, 2017, New York, NY, ISBN: 978-1-259-12991-9.
[43] Morelli, E.A. and Klein, V. *Aircraft System Identification: Theory and Practice, 2nd*, Sunflyte Enterprises, 2016, Williamsburg, VA, USA, ISBN: 9780997430615.
[44] Deiler, C., Ohme, P., Raab, C., Mendonca, C. and Silva, D. Facing the challenges of supercooled large droplet icing: results of a flight test based joint DLR-embraer research project, *SAE Int. J. Adv. Curr. Pract. Mob.*, 2019, **2**, pp 192–204. ISSN: 2641-9645. https://doi.org/10.4271/2019-01-1988
[45] Deiler, C. Comparison of flight characteristics of two different airplanes and ice configurations, *J. Aircraft*, 2020, **57**, pp 995–1000. https://doi.org/10.2514/1.C035801
[46] Bragg, M.B., Broeren, A.P. and Blumenthal, L.A. Iced-airfoil aerodynamics, *Prog. Aerosp. Sci.*, 2005, **41**, pp 323–362. https://doi.org/10.1016/j.paerosci.2005.07.001
[47] Coates, E.M., Reinhardt, D., Gryte, K., & Johansen, T.A. Toward nonlinear flight control for fixed-wing UAVs: system architecture, field experiments, and lessons learned, in *2022 International Conference on Unmanned Aircraft Systems (ICUAS)*, 2022, pp 724–734. https://doi.org/10.1109/icuas54217.2022.9836064
[48] Ljung, L. *System Identification: Theory for the User, 2nd*, Prentice Hall PTR, 1999, Upper Saddle River, N.J, ISBN: 0136566952.
[49] Forssell, U. and Ljung, L. Closed-loop identification revisited, *Automatica*, 1999, **35**, pp 1215–1241. https://doi.org/10.1016/S0005-1098(99)00022-9
[50] Ågren, T.S., Ruan, A.W., Malpica, C., Withrow-Maser, S. and Meyn, L. In-flight system identification of the ingenuity Mars helicopter, *J. Guid. Control Dyn.*, 2026, **49**, pp 1005–1022. https://doi.org/10.2514/1.G009064
[51] Stull, R.B. *An Introduction to Boundary Layer Meteorology, 1st ed*, Springer Dordrecht, 1988, Netherlands, ISBN: 978-90-277-2768-8. https://doi.org/10.1007/978-94-009-3027-8
[52] Larson, T.J., Evaluation of a flow direction probe and a pitot-static probe on the F-14 airplane at high angles of attack and sideslip, *Tech. rep. NASA*, 1984.
[53] Jategaonkar, R.V. *Flight Vehicle System Identification: A Time Domain Methodology, 2nd ed*, AIAA, 2015, Reston, VA, USA, ISBN: 9781624102783. https://doi.org/10.2514/4.102790
[54] Deiler, C., Mönnich, W., Seher-Weiß, S. and Wartmann, J. Retrospective and recent examples of aircraft and rotorcraft system identification at DLR, *J. Aircraft*, 2023, **60**, pp 1371–1397. https://doi.org/10.2514/1.C037262
[55] Tian, P., Chao, H., Flanagan, H.P., Hagerott, S.G. and Gu, Y. Design and evaluation of UAV flow angle estimation filters, *IEEE Trans. Aerosp. Electron. Syst.*, 2019, **55**, pp 371–383. https://doi.org/10.1109/TAES.2018.2852359

Downloaded from https://www.cambridge.org/core. 28 Sep 2026 at 04:58:16, subject to the Cambridge Core terms of use.

[56] Etkin, B. and Reid, L.D. *Dynamics of Flight: Stability and Control, 3rd ed*, John Wiley & Sons, 1996, New York, NY, ISBN: 0-471-03418-5.
[57] Oo, N.L., Richards, P.J. and Sharma, R.N. Ice-induced separation bubble on RG-15 airfoil at low Reynolds number, *AIAA J.*, 2020, **58**, pp 5156–5167. https://doi.org/10.2514/1.J059257
[58] Fischenberg, D. Identification of an unsteady aerodynamic stall model from flight test data, in *20th Atmospheric Flight Mechanics Conference*, 2012. https://doi.org/10.2514/6.1995-3438
[59] Gülçat, Ü. *Fundamentals of Modern Unsteady Aerodynamics, 3rd ed*, Springer Cham, 2021, Switzerland, ISBN: 978-3-030-60777-7. https://doi.org/10.1007/978-3-030-60777-7
[60] Løw-Hansen, B., Hann, R. and Lindner, M.J. *Flight-test system identification of leading-edge rime-ice effects on a small fixed-wing UAV*, Version V1, 2026. https://doi.org/10.18710/NNHVBP

Cite this article: Løw-Hansen B., Lindner M., Johansen T. A., Hann R. and Deiler C. UAV icing: system identification of leading-edge rime-ice effects on a small fixed-wing drone. *The Aeronautical Journal*, https://doi.org/10.1017/aer.2026.10234

Downloaded from https://www.cambridge.org/core. 28 Sep 2026 at 04:58:16, subject to the Cambridge Core terms of use.